Neuron

Article

Topography of putative bi-directional interaction between hippocampal sharp-wave ripples and neocortical slow oscillations

Graphical abstract

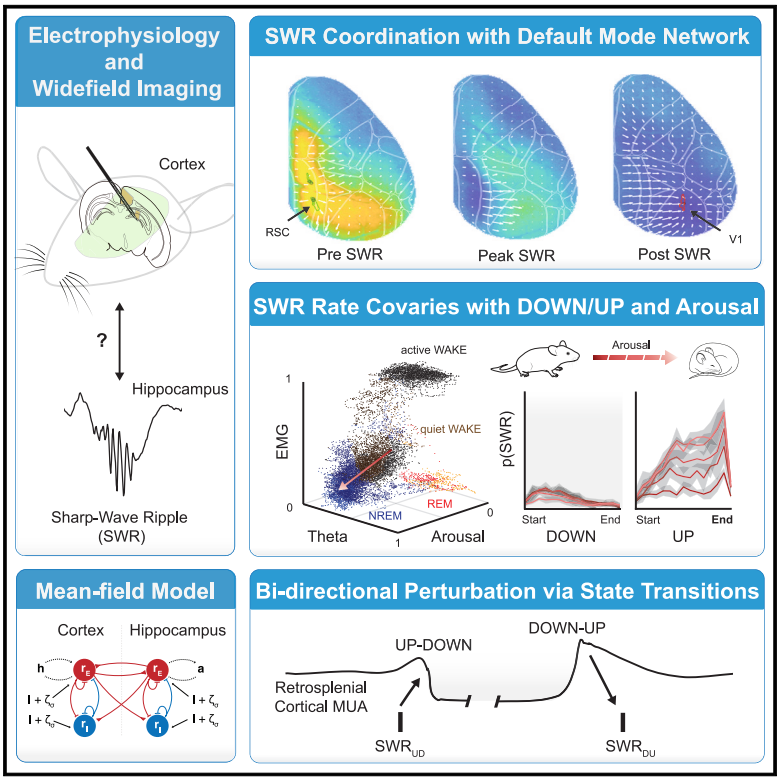

Authors

Rachel A. Swanson, Elisa Chinigò, Daniel Levenstein, ..., Xiao-Jing Wang, Jayeeta Basu, György Buzsáki

Correspondence

jayeeta.basu@nyulangone.org (J.B.), gyorgy.buzsaki@nyulangone.org (G.B.)

In brief

Mechanisms of hippocampal-mediated systems consolidation across neocortex remain unknown. Swanson et al. suggest the hippocampus and retrosplenial cortex are weakly coupled, excitable systems capable of state-dependent, bi-directional perturbation. Retrosplenial cortex may further act as a gateway through which SWRs can perturb downstream cortical regions via propagation of DOWN states.

Highlights

- Hippocampal sharp-wave ripple rate is modulated by neocortical UP/DOWN states
- Mean-field model predicts hippocampus and neocortex as weakly coupled excitable systems
- Sharp-wave ripples can trigger DOWN states, DOWN-UP transitions can trigger ripples
- Ripple perturbation of the cortex invades large areas via propagation of DOWN states

Swanson et al., 2025, Neuron *113*, 754–768
March 5, 2025
https://doi.org/10.1016/j.neuron.2024.12.019

CellPress

CellPress

Neuron

Article

Topography of putative bi-directional interaction between hippocampal sharp-wave ripples and neocortical slow oscillations

Rachel A. Swanson,[1] Elisa Chinigò,[5] Daniel Levenstein,[6,7] Mihály Vöröslakos,[1] Navid Mousavi,[1] Xiao-Jing Wang,[5] Jayeeta Basu,[1,2,4,*] and György Buzsáki[1,2,3,8,*]

[1]Neuroscience Institute, Langone Medical Center, New York University, New York, NY, USA
[2]Department of Physiology and Neuroscience, Langone Medical Center, New York University, New York, NY, USA
[3]Department of Neurology, Langone Medical Center, New York University, New York, NY, USA
[4]Department of Psychiatry, Langone Medical Center, New York University, New York, NY, USA
[5]Center for Neural Science, New York University, New York, NY, USA
[6]Department of Neurology and Neurosurgery, McGill University Montreal, QC, Canada
[7]Mila – The Quebec AI Institute, Montreal, QC, Canada
[8]Lead contact
*Correspondence: jayeeta.basu@nyulangone.org (J.B.), gyorgy.buzsaki@nyulangone.org (G.B.)
https://doi.org/10.1016/j.neuron.2024.12.019

SUMMARY

Systems consolidation relies on coordination between hippocampal sharp-wave ripples (SWRs) and neocortical UP/DOWN states during sleep. However, whether this coupling exists across the neocortex and the mechanisms enabling it remains unknown. By combining electrophysiology in mouse hippocampus (HPC) and retrosplenial cortex (RSC) with wide-field imaging of the dorsal neocortex, we found spatially and temporally precise bi-directional hippocampo-neocortical interaction. HPC multi-unit activity and SWR probability were correlated with UP/DOWN states in the default mode network (DMN), with the highest modulation by the RSC in deep sleep. Further, some SWRs were preceded by the high rebound excitation accompanying DMN DOWN → UP transitions, whereas large-amplitude SWRs were often followed by DOWN states originating in the RSC. We explain these electrophysiological results with a model in which the HPC and RSC are weakly coupled excitable systems capable of bi-directional perturbation and suggest that the RSC may act as a gateway through which SWRs can perturb downstream cortical regions via cortico-cortical propagation of DOWN states.

INTRODUCTION

Theories of systems consolidation rely on hippocampal-mediated coordination of neural activity across the neocortex in service of reactivation during sleep.[1–5] However, how and to what extent this spontaneously occurs across regions, often many synapses removed from the hippocampus (HPC), remains unknown. During NREM sleep, neural populations alternate between periods of spiking and inactivity, termed UP and DOWN states in the neocortex, and sharp-wave ripples (SWRs) and inter-SWRs (iSWRs) in the HPC. Both gain- and loss-of-function studies demonstrate the importance of the tight temporal coordination of these events for systems consolidation.[6,7] However, the observed timing of this coordination is variable across experiments and regions, leading to a lack of mechanistic consensus regarding the inter-regional interaction required for consolidation.

Most studies agree that the probability of SWRs is higher during UP states and that the spike content of SWRs is biased by neocortical inputs,[8–13] but see [14–16]. Some studies further suggest that SWRs initiate neocortical UP states,[14,17,18] whereas others, in contrast, indicate that DOWN states follow SWRs.[11,12,19] These discrepancies may be due to variation in sleep depth, which modulates the rate of both SWRs and DOWN states,[14,20–23] or differences between cortical regions, especially given that UP/DOWN states can be localized[24] or travel across the forebrain.[25,26]

In an attempt to resolve these ambiguities, imaging studies have explored the topographic relationship between SWRs and the rest of the brain. In primates, SWRs were correlated with an increase in the blood-oxygen-level-dependent (BOLD) signal in regions comprising the default mode network (DMN),[23,27] similarly observed in humans using MEG.[28] Although of functional interest given the importance of the DMN for episodic recall,[29,30] only recently have rodent wide-field imaging studies had the spatiotemporal resolution necessary to explore short timescale interaction between the HPC and dorsal

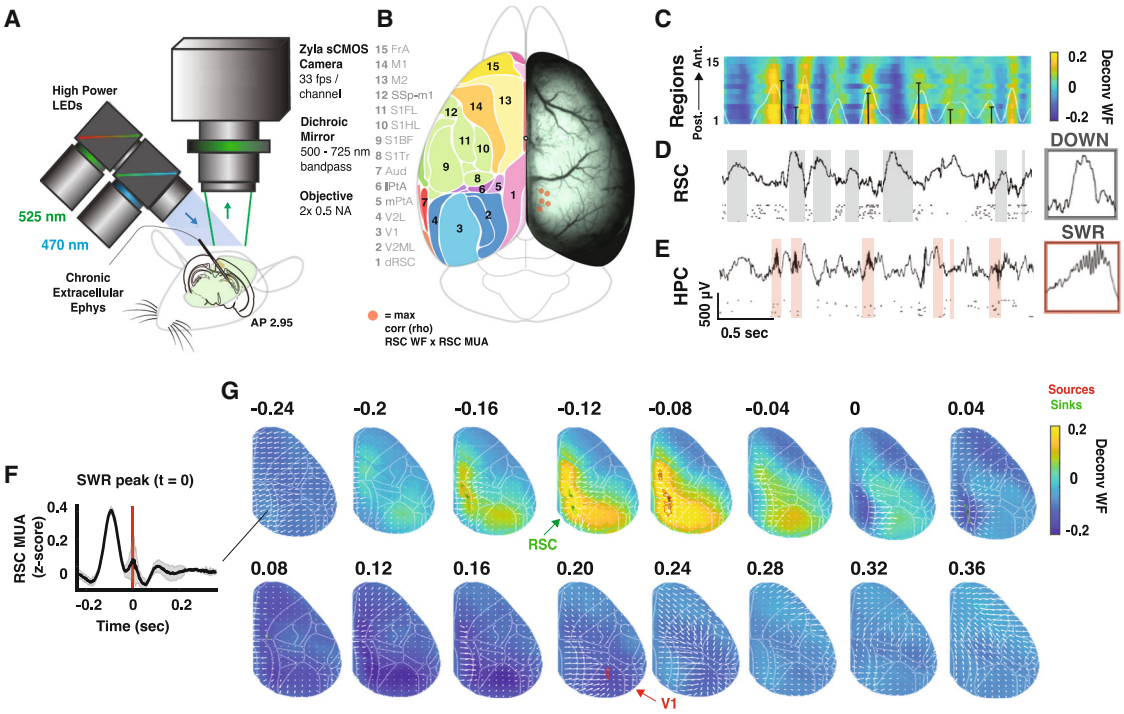

Figure 1. Experimental preparation and neocortical activity surrounding hippocampal SWRs

(A) Dual wavelength (blue 470 nm—thy1 GCaMP6f; green 525 nm—total blood volume) wide-field imaging (66 frames per second) of the dorsal hemisphere of a thy1 GCaMP6f mouse. Note chronic silicon probe spanning ipsilateral CA1 and RSC beneath the imaging field of view (green).

(B) Right, example raw fluorescence frame. Left, corresponding cortical regions. Red dots indicate location of maximum correlation (rho) between wide-field signal and RSC population rate for each mouse (n = 5).

(C–E) Aligned simultaneous wide-field imaging of dorsal cortex and electrophysiological recordings in the HPC and RSC. (C) Deconvolved wide-field time series for 15 pixels in regions ranging from posterior to anterior dorsal cortex as in (B). White line corresponds to RSC wide-field time series (also row 1 in heatmap); black bars denote SWRs, height proportional to SWR amplitude. (D and E) Example LFP and single units from RSC and hippocampal CA1 pyramidal layer. Shaded areas highlight DOWN states and SWRs in RSC and HPC, respectively. Right insets, example DOWN state and SWR (100 ms).

(F) Average RSC MUA (see STAR Methods) surrounding all SWR peaks at t = 0. Shading corresponds to standard deviation across mice (n = 5).

(G) Average deconvolved wide-field activity across all mice surrounding SWR peak at t = 0. Sources and sinks are identified in green and red, respectively. Arrows correspond to vector fields calculated across pairs of frames on the grand-average video, providing a qualitative view of activity flow.

neocortex, with variable results.[31–33] Thus, where, when, and how SWRs are coupled with neocortical UP/DOWN states remains an unresolved tension across theories of systems consolidation.

Toward this goal, we developed a chronic preparation in mice that combined wide-field imaging in the dorsal neocortex with silicon probe recordings of the HPC and retrosplenial cortex (RSC) in the same hemisphere. We found a topographically specific, state-dependent, bi-directional interaction between hippocampal SWRs and neocortical UP/DOWN states. From the neocortex to the HPC, SWRs were less likely to occur during DOWN states across regions in the DMN, and SWRs often followed large rebound excitation at the DOWN-UP transition in DMN. From the HPC to the neocortex, large-amplitude SWRs were often followed by DOWN states in the RSC and motor cortical regions that then propagated along the dorsal neocortex. The highest modulation was seen in the RSC during deep NREM sleep in all cases. We hypothesized that these experimental observations could arise from weakly coupled populations in the complementary excitable regimes characteristic of NREM[34] and confirmed the plausibility of this hypothesis with a mean-field model of bi-directionally interacting hippocampal and RSC populations.

RESULTS

Combined wide-field imaging and chronic extracellular electrophysiology for studying hippocampal-cortical interaction during sleep

We combined chronic electrophysiological recordings from the HPC and RSC, a neocortical region involved in spatial cognition and implicated in systems consolidation,[35–39] with wide-field imaging of the dorsal neocortex in head-fixed Thy1 GCaMP6f mice (Figure 1A).[40] To record concurrently in the same hemisphere, a single-shank silicon probe (64 or 128 recording sites) was lowered through the left hemisphere to the right RSC and hippocampal CA1 regions, ipsilateral to our thinned-skull cranial window preparation (Figures 1A–1E). Following hemodynamic correction (Ma et al.[41]; see STAR Methods) and alignment of wide-field videos to the Allen Institute's Common Coordinates Framework

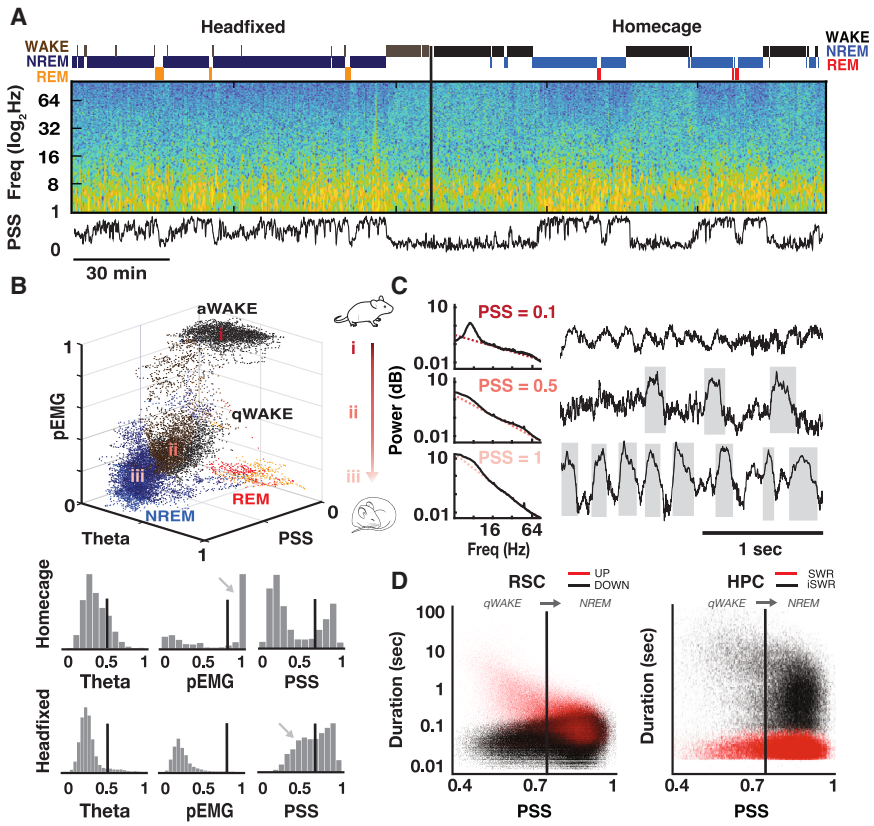

Figure 2. SWR and DOWN state rates increase as animals move from quiet wake to deep NREM sleep

(A) Brain-state scoring of concatenated head-fixed and home-cage recording sessions for an example mouse. Top, identified WAKE, NREM, and REM states. Middle, spectrogram of RSC LFP. Bottom, time-varying slope of the power spectrum (PSS).

(B) Top, state scoring of the session in (A). Note three distinct clusters, classified as active wake (aWAKE), REM sleep, and a third cluster with continuous variation from quiet wake (qWAKE) to NREM sleep. Bottom, distributions of the three variables used for behavioral-state scoring (PSS, pseudo EMG, and theta power) in homecage and head-fixed conditions.

(C) Average RSC power spectra (black; left) and example RSC LFP traces (right) at three different arousal levels from active WAKE to deep NREM, denoted (i)–(iii) in (B) scatterplot. Inset PSS values are the inverse of the slope of the linear fit to the aperiodic component of the power spectra (pink dotted lines). DOWN states are shaded in gray.

(D) Left, scatterplot of durations of UP (red) and DOWN (black) states in the RSC across values of PSS for all mice. Right, scatterplot of dwell time durations for SWRs (red) and iSWR periods (black). Vertical lines in the RSC and HPC separate qWAKE and NREM.

(Figure S1; Wang et al.[42]; see STAR Methods), we confirmed the successful placement of our recording electrode by verifying that the correlation between the extracellularly recorded RSC population rate and all wide-field pixels was highest in the RSC (Figure 1B, red dots). To recover fine timescale changes in the population rate across our imaging field of view, we determined a deconvolution kernel that optimally predicted the electrically recorded RSC population rate from the identified RSC region of interest (ROI) in each mouse (Figure S2; Video S1; Peters et al.[43]; see STAR Methods). We next deconvolved wide-field activity across the neocortex for each mouse with the derived kernel, as was successfully done previously.[43] Variation in standard deviation of deconvolved pixel time series across regions was minimal (Figure S2). The remaining analyses were performed with either deconvolved wide-field activity or unaltered fluctuations in total blood volume (total hemoglobin [Hbt]; 525 nm), as specified. This approach uniquely combined optical measurement of the population rate of excitatory cells across the dorsal neocortical mantle (Figures 1B and 1C) with simultaneous extracellular recordings in the HPC and RSC in the same hemisphere (Figures 1D and 1E).

As observed electrophysiologically (Figure 1F; peak time t = 0, cites), SWRs were preceded by elevated neocortical activity in the deconvolved wide-field data (Figure 1G; Video S2), led by a source in RSC (t = −0.12 s) that spread throughout midline-posterior cortical regions (mouse DMN or "medial networks"[44]). This increased activity was followed by decreased activity in the RSC that spread across the neocortex, ultimately terminating with a sink in V1 (t = 0.2 s).

Joint fluctuation of SWRs and cortical DOWN states across ultraslow (0.01–0.03 Hz), infraslow (0.04–0.5 Hz), and slow (0.5–4 Hz) timescales

Next, we examined whether hippocampal-cortical coupling varied as animals shifted from wake to sleep. Automated classification of brain states was performed using three variables: the time-varying slope of the RSC power spectrum (power spectral slope [PSS]),[45] HPC theta power, and LFP-derived electromyogram (EMG) (pseudo-EMG) (Figures 2A and 2B).[20,46] This resulted in 3 clusters that corresponded to active WAKE (high EMG), REM, and a third cluster that ranged from quiet WAKE (low EMG) to NREM (Figure 2B). To ensure that the brain states observed during head-fixation were comparable with natural behavior, we state-scored concatenated head-fixed and home-cage recording sessions within the same mouse (Figures 2A and 2B). Although the fraction of time spent in each state varied between conditions, the regular recurrence of transitions from deep NREM to REM sleep in both conditions and the qualitatively overlapping head-fixed and home-cage brain state clusters confirmed comparable sleep quality in head-fixed animals (Figure S3 for individual mice).

Hippocampal SWRs and RSC UP/DOWN states were observed exclusively throughout the brain state cluster comprised of quiet WAKE and NREM sleep (labeled ii and iii in

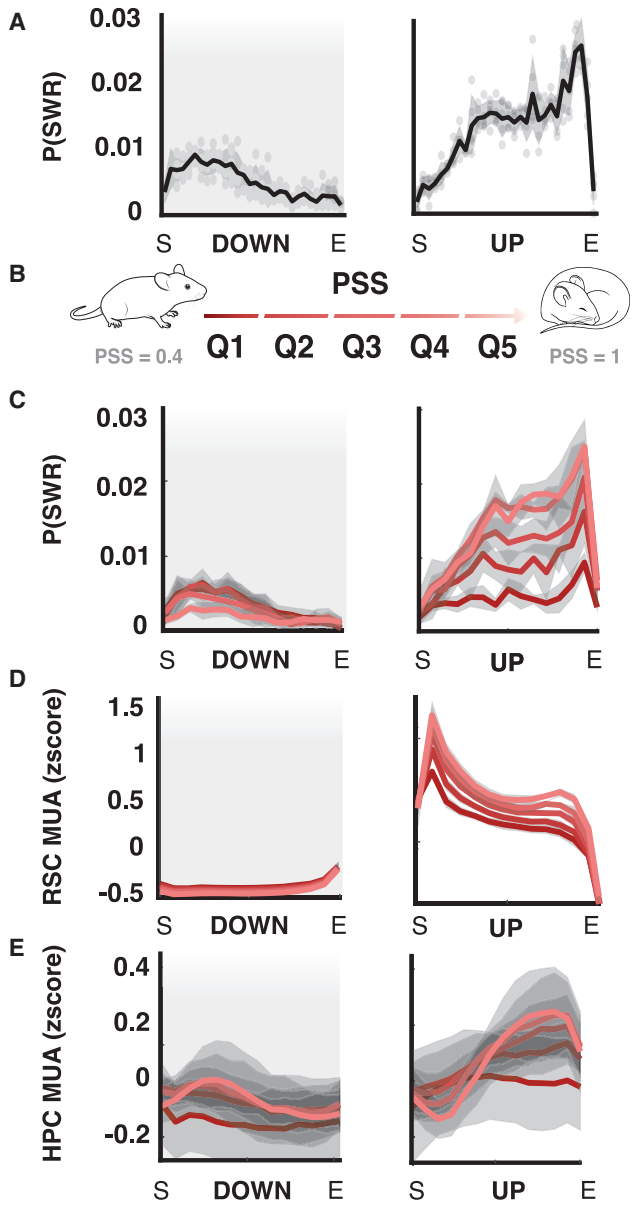

Figure 3. SWR rate co-varies with RSC UP and DOWN states as a function of brain state

(A) Probability of SWRs across time-normalized RSC UP and DOWN states. Shading corresponds to standard deviation across mice; dots to individual mice. S, start of state; E, end of state.

(B) PSS quintiles span quiet WAKE to deep NREM (Q1–Q5; colored from dark to light red in all panels).

(C–E) Variables specified plotted across time-normalized RSC UP and DOWN states as a function of PSS quintile; all mice. Shading corresponds to standard deviation across all UP or all DOWN states. (C) Probability SWR by PSS quintile. (D) Mean RSC MUA by PSS quintile. (E) Mean HPC MUA by PSS quintile.

Figure 2B). However, their frequency of occurrence varied continuously as a function of PSS or arousal level (Figure 2C).[47] From quiet WAKE (low PSS) to deep NREM sleep (high PSS), the DOWN state rate increased (Figure 2C). This occurred because the duration of RSC UP states got increasingly shorter (Figure 2D, left red) and the duration of DOWN states became increasingly more variable (Figure 2D, left black), until the ratio of mean UP and DOWN state durations approached one. The HPC followed a complementary pattern: as PSS values increased, the rate of hippocampal SWRs increased due to a decrease in the iSWR interval (Figure 2D right black).

Hippocampal SWRs also co-varied with RSC UP and DOWN states, with SWRs significantly more likely during UP states (Figure 3A). This relative change in SWR rate from DOWN to UP (D-U) states increased monotonically with increasing PSS, ultimately resulting in a 3-fold increase in SWR rate from D-U states during deep NREM (Figures 3B and 3C), parallel with increased RSC multi-unit activity (MUA) within UP states (Figure 3D). Hippocampal MUA likewise increased with increasing RSC UP state firing rate, following RSC D-U transitions with a time lag despite a near-synchronous decrease in RSC rate at the UP to DOWN (U-D) transition (Figure 3E; "co-active and co-silent frames").[9,10,15] In sum, the modulation of hippocampal activity by RSC UP/DOWN states depended on arousal level, as measured by PSS. With decreasing arousal, the mean firing rate of RSC UP states increased and was paralleled by an increase in HPC MUA and subsequent increased probability of SWRs.

Brain state, as measured using a variety of metrics, is known to fluctuate in both the "ultraslow" (0.01–0.03 Hz) and "infraslow" (0.04–0.5 Hz) frequency bands[48–52] (apparent in cortical blood flow[53,54]). Enabled by green wavelength (525 nm) imaging of total blood volume (Hbt) across the neocortical mantle, we found that fluctuations in Hbt showed a 1/f background, with peaks in the ultraslow and infraslow frequency ranges (Figure S4; Video S3). Variation in PSS more closely tracked fluctuation in the ultraslow-filtered Hbt (Figure S4D), which was globally coherent across the cortical mantle (Figure S4E). In contrast, the infraslow-filtered Hbt was accompanied by a faster-timescale modulation of SWR rate, confined to the DMN (Figure S4F).[28] This phase-dependence was not restricted to SWRs but rather reflected a broader infraslow-timescale switch in RSC and HPC LFP between power spectra typical of the NREM to a state dominated by 4 Hz in the RSC (Figure S4G).

Together, these results reveal co-modulation of the hippocampal-cortical state at three timescales: (1) an ultraslow (0.01–0.03 Hz) variation in brain state (perhaps analogous to the "global signal" in fMRI,[55,56] measured by the time-varying slope of the power spectrum (PSS) and fluctuations in total blood volume (Hbt) and accompanied by concurrent changes in the rate of DOWN states, SWRs, and cortical spiking activity during UP states; (2) an infraslow (0.04–0.5 Hz) fluctuation of cortical state in mouse DMN (perhaps reflecting excitability changes during NREM sub-stages or "packets"[20] ; and (3) a slow (.5–4 Hz) modulation of SWR rate by RSC UP and DOWN states.

Putative bi-directional hippocampal-cortical perturbation by transient population synchrony

Motivated by previously observed temporal coupling between SWRs and cortical slow waves,[12,57] and the finding that SWRs cluster toward the end of time-normalized UP states (Figures 3A and 3C), we next investigated whether UP/DOWN

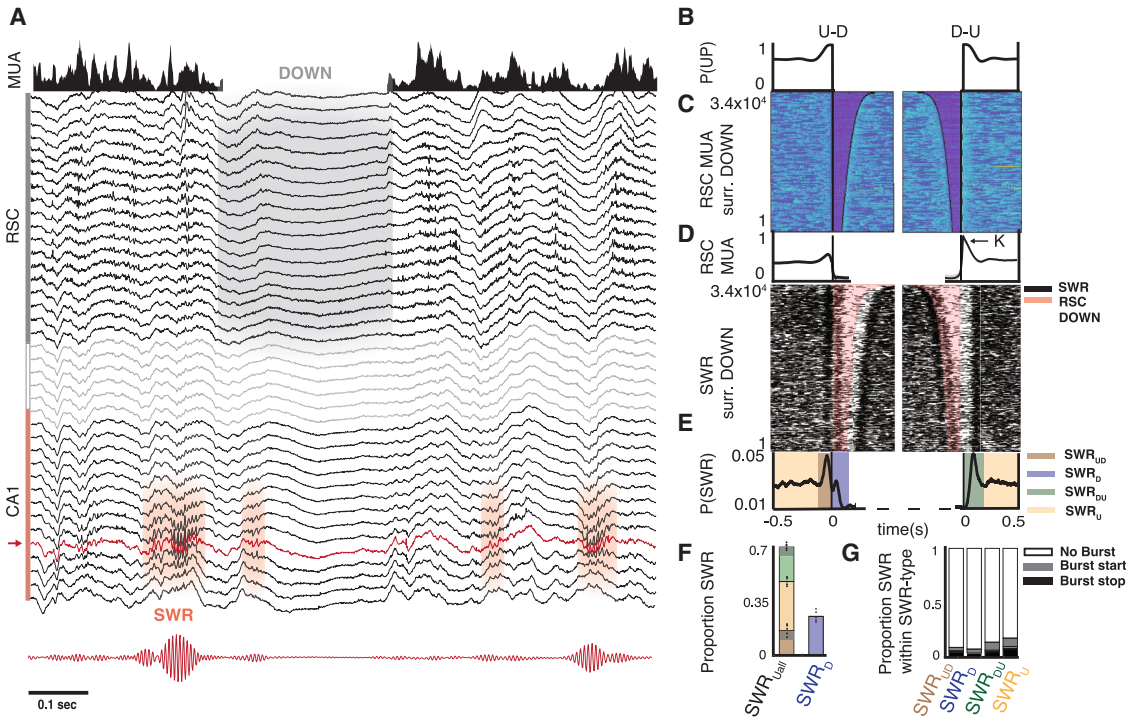

Figure 4. Probability of SWRs around U-D and D-U transitions is asymmetric

(A) Example LFP traces spanning layers of granular RSC, white matter, and ipsilateral CA1; RSC MUA (above); ripple-frequency-filtered CA1 trace (below; 130–200 Hz; bandpass filtered channel designated in red).

(B–E) Data specified surrounding all DOWN states for an example mouse, centered at RSC U-D transitions (left) or D-U transitions (right) and sorted by DOWN state duration. (B) Probability of being in an UP state, surrounding transitions. (C) RSC MUA; each row is a U-D (left) or D-U (right) transition (>30,000). Bottom, average RSC MUA surrounding transition specified. K refers to transient rebound population synchrony at the D-U transition, K-complex or "K."

(D) Raster plot of all SWRs during the same RSC U-D and D-U transitions as in (C). Pink shading corresponds to RSC DOWN states identified in (C). SWRs plotted as thin black lines, the length of which corresponds to their durations. Note decreased P(SWR) during DOWN, asymmetry in clustering of SWRs around transitions, and change in clustering as DOWN duration increases.

(E) Defining SWRs by their temporal proximity to U-D and D-U transitions yields 4 types: SWR_U (yellow), SWR_{UD} (red), SWR_D (blue), and SWR_{DU} (green); see STAR Methods and Figure S6.

(F) Proportion of each "SWR type" across all mice (dots represent individual mice; colors correspond to SWR type). Note 3-fold increase in SWR rate from D-U states. Gray shaded region in SWR_{UD} and SWR_{DU} represents the overlap between these categories (~30%).

(G) For each SWR type, proportion of those SWRs that occur in bursts vs. not in bursts (see STAR Methods). Start and end times of the burst are denoted by gray and black.

state transitions in the RSC could predict the timing of SWRs. When aligned to D-U or U-D transitions (Figures 4B–4D), RSC MUA was asymmetric, displaying a peak at the D-U transition not present at the U-D transition (putative K-complex, K; Figure 4D). In parallel, we observed a tight clustering of SWRs around U-D and D-U transitions, with probability of SWR occurrence (pSWR) exhibiting three distinct peaks (Figures 4D and 4E). First, a peak in pSWRs occurred within a 50-ms time window prior to the U-D transition (SWR_{UD}). Second, pSWR peaked within ~80 ms after the U-D transition (SWR_D). Finally, a peak in pSWR occurred after an ~120-ms delay after the D-U transition in the RSC (SWR_{DU}) following the D-U peak in RSC MUA. There were many more U-D and D-U state changes than the number of SWRs, so these hypothesized interactions took place during only a small fraction of cortical transitions. Nevertheless, more than half of the SWRs were time-locked to RSC D-U or U-D state transitions (SWR_{UD}, SWR_{DU}, and SWR_D types; Figure 4I; Figure S5). Although SWR bursts (defined as an iSWR interval of 50–132 ms) comprised only a small fraction (<20%) of all SWRs, burst onsets were more likely following the D-U transition (SWR_{DU}) and burst offsets were more likely at the U-D transition (SWR_{UD}), particularly surrounding long DOWN states (Figure S5). These observations cannot simply be explained by tonic modulation of the SWR rate by UP states, as UP state probability is symmetric surrounding U-D and D-U transitions (Figure 4B).

The clustering of SWRs around U-D and D-U transitions suggests a more temporally precise, and potentially causal, hippocampal-neocortical interaction, whereby hippocampal SWRs may induce U-D transitions in the cortex and the transient elevation of cortical MUA at D-U transitions (K-complex) may induce SWRs in the HPC (Figure 5A).[15,18,34] To test this possibility further, we examined the change in the probability of RSC DOWN states as a function of SWR amplitude (Figure 5B) and the change in the probability of SWRs as a function of K-complex magnitude, defined as average RSC MUA within a 20-ms window following the D-U transition (Figure 5E). As the

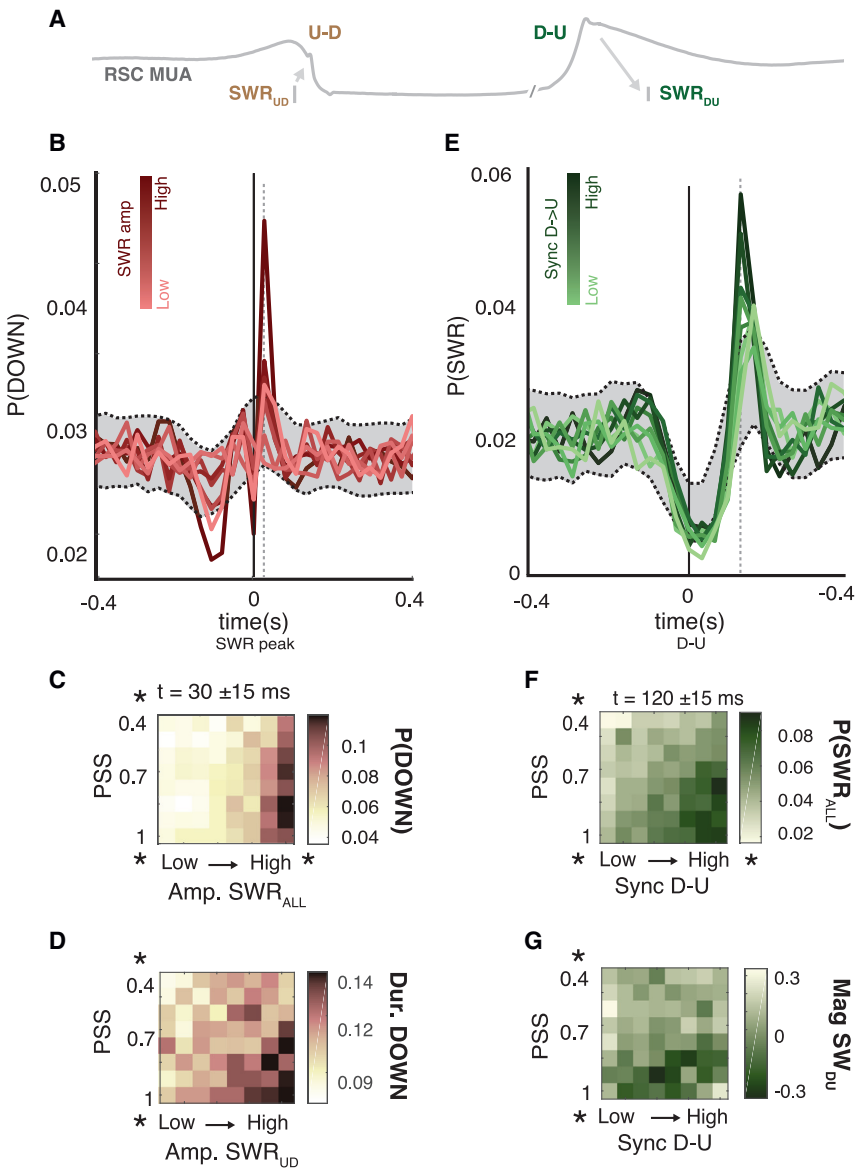

Figure 5. Temporal relationship between HPC and RSC state transitions is state-dependent and bi-directional

(A) Schematic of hypothesis: SWRs can induce U-D transitions and D-U transitions can induce SWRs, conditional on magnitude of the perturbation and state of the receiving region.

(B) Cross-correlograms between SWR peaks (t = 0 s) and DOWN state onsets across all mice, colored by SWR amplitude octile (light to dark red; small to large SWRs). Shading denotes boot-strapped 99% confidence intervals obtained by shuffling both SWR_{ALL} peak and U-D time series by ±30 ms, 1,000 iterations. Note increased probability of DOWN onset at fixed 30 ± 15-ms timelag (vertical gray line) with increasing SWR amplitude.

(C) Mean probability of DOWN state onset at a 30-ms lag from SWR peak, timelag of putative "interaction" as a function of depth of sleep (PSS) and SWR_{ALL} amplitude (repeated measures two-way ANOVA across sessions [n = 15]: R2 = 0.47. *SWR amplitude*, F = 83.19, $p < 0.001$, $\eta^2p = 0.42$; *PSS*, F = 5.87, $p < 0.001$, $\eta^2p = 0.07$; *interaction*, F = 1.68, $p < 0.05$, $\eta^2p = 0.06$). Significant effect of amplitude SWR, depth of sleep, and their interaction. Note the significant effect of *SWR amplitude* is driven by amplitude octiles 7 and 8.

(D) Mean duration of DOWN states following SWR_{UD} as a function of depth of sleep (PSS) and SWR_{UD} amplitude across all mice (GLM 5-fold CV: R2 = 0.014. *SWR amplitude* β1 = −0.007, t = 0.006, p = *NS*; *PSS* β1 = 0.067, t = 7.68, $p < 0.001$; *interaction* β1 = −0.016, t = 1.96, $p < 0.05$).

(E) Probability of SWRs surrounding RSC D-U transitions (t = 0 s), colored by D-U rebound excitation octile (light to dark green, small to large). Note increase in P(SWR) with increasing rebound excitation at a fixed lag of 120 ms (vertical gray line). Confidence intervals computed as in (B).

(F) Mean probability of SWR occurrence at a 120-ms lag from RSC D-U as a function of depth of sleep (PSS) and D-U rebound excitation (repeated measures two-way ANOVA: R2 = 0.58. *Rebound excitation*, F = 54.01, $p < 0.001$, η^2p = 0.32; *PSS*, F = 120.26, $p < 0.001$, $\eta^2p = 0.42$; *interaction*, F = 3.78, $p < 0.001$, $\eta^2p = 0.15$.

(G) Mean magnitude of HPC sharp-waves as a function of tonic MUA HPC and D-U rebound excitation across all mice (GLM 5-fold CV: R2 = 0.05. *Rebound excitation* β1 = −0.27, t = −1.65, p = *NS*; *PSS* β1 = −1.01, t = −5.02, $p < 0.001$; *interaction* β1 = 0.4, t = 1.95, $p < 0.05$).

amplitude of SWRs increased, they were more likely to be followed by a U-D transition at a fixed 30 ±15-ms delay (Figure 5B). The consistency of this lag suggests it is the time window in which hypothesized SWR-induced DOWN states occur. Similarly, as MUA at the D-U transition increased, the probability of SWRs increased at a fixed lag of 120 ± 15 ms (Figure 5E), suggesting the lag at which K-complex induction of SWRs may occur.

We further found that the interaction between SWRs and UP-DOWN states was modulated by arousal level, as measured by PSS. Large-amplitude SWRs were more likely to be followed by DOWN states in deep NREM (high PSS), with a significant effect of SWR amplitude, PSS, and their interaction (Figure 5C). In addition, we found a significant effect of arousal level and the interaction of arousal level with SWR amplitude on DOWN duration (Figure 5D), implying the duration of DOWN states is conditional on depth of sleep and providing further support for a potential role of SWRs in DOWN state induction. Similarly, K-complex magnitude increased the probability of SWRs at a fixed lag of 120 ± 15 ms, with a significant effect of magnitude K-complex, PSS, and their interaction (Figure 5F). Further, the magnitude of sharp wave sink in stratum radiatum, a measure of the input drive to CA1 from CA3, became increasingly negative (corresponding to a larger sink) as a function of PSS and interaction of PSS with K-complex magnitude (Figure 5G). Overall, these findings support the hypothesis that large-amplitude SWRs may trigger U-D transitions (SWR_{UD}) and that transient spike synchrony at D-U transitions (K-complex) may trigger

SWRs (SWR_{DU} and a fraction of SWR_D when UP state is short; <100 ms). In both directions, the effectiveness of the transient burst in spiking activity accompanying SWRs and D-U transitions depended on the state of the target region, which varied with sleep depth as operationalized by PSS.

Modulation of SWR rate by DOWN states is restricted to mouse DMN

We next asked whether the putative bi-directional interaction observed between HPC and RSC extended to other neocortical regions. We first binarized our wide-field data into UP and DOWN states using a pixel-wise 25th percentile cut-off, which produced the best alignment of extracellularly and optically detected DOWN states in the RSC (Figure S7A). We then plotted deconvolved wide-field activity (Figure 6Bi), RSC MUA (Figure 6Bii), and SWR incidence (Figure 6Biii) surrounding these DOWN states in 7 selected neocortical regions (Figure 6A), spanning medial networks (or DMN; red) and somatic sensorimotor networks (blue; networks as determined anatomically in Zingg et al.[44]). Although DOWN states were reliably detected across these regions (Figure 6Bi; Figure S7F, dotted lines), RSC MUA only followed wide-field-detected DOWN states in RSC and regions in mouse medial or default mode networks, as expected given their dense anatomical connectivity (Figure 6Bii; Figure6Ci; Figures S7D–S7F). Paralleling this, a decrease in SWR rate was observed during DOWN states detected across the medial network (positive SWR modulation index; see STAR Methods; Figure 6Cii) but not somatic sensorimotor networks. This effect was pronounced, with longer DOWN state duration (Figure S7G), which occupied a greater cortical area.

To examine DOWN state topography surrounding SWRs, we plotted the average probability of DOWN states surrounding SWR peaks, separated by small- and large-amplitude SWRs (Figures 7Ai and 7Bi; t = 0 s). Consistent with our electrophysiological and optical observations (Figures 1 and 5), SWRs were preceded by a significant increase in UP state probability, localized to the mouse medial network, beginning 120 ms before SWR occurrence (Figures 7A and 7B, red). Whereas small-amplitude SWRs occurred during a DOWN state that remained largely confined to the RSC, large-amplitude SWRs occurred during UP states and were followed by DOWN states in the RSC and lateral M1/M2 (Figure 7Bi, arrows at 30 ms; Figure 7Bii, white outlines) that then spread across the neocortex, as measured by a shift in DOWN onset latencies across adjacent cortical regions (Figure 7Bii). DOWN state onset in the RSC was followed by DOWN states in visual and somatosensory regions (Figure 7Bii, white to blue outlines). DOWN state onset in M2 and M1 was followed by DOWN states in midline prefrontal, anterior cingulate, and somatosensory regions. DOWN states terminated in the V1 and barrel cortex. This suggests that large-amplitude SWRs are followed by DOWN states initiated in RSC and/or M1/M2 that then invade much of the neocortex with trajectories following cortico-cortical anatomical connectivity (see Video S4).

To examine the topography of K-complex impact on hippocampal SWRs, we plotted the average probability of SWRs surrounding the DOWN-UP transition for every pixel (Figure 7Ci; t = 0 s). A sustained decrease in the probability of SWRs following the D-U transition was observed across the medial network, followed by a peak in SWR probability at ~120 ms after D-U transitions in the RSC that spread toward visual areas, eventually returning to the RSC (Figures 7Ci and 7Ciii; Video S5). Average wide-field activity at the D-U transition was greater in the medial network than in somatic sensorimotor networks (Figure 7Cii), paralleling the regions for which SWRs were time-locked to D-U transitions.

Model of weakly coupled excitable systems accounts for hippocampal-retrosplenial interactions

We hypothesized that the interactions observed between hippocampal SWRs and RSC DOWN states result from weakly coupled excitable systems.[34] We modeled RSC and HPC each as an adapting inhibition-stabilized network (aISN, Figure 8A, see STAR Methods)[58] with slow feedback on excitatory activity,[34,59] corresponding to adaptation in the HPC[60,61] and I_h in the cortex.[62–64]

In the presence of noise, the aISN model generates alternation dynamics with asymmetric durations of UP/DOWN states in the RSC and SWRs/iSWR intervals in the HPC (Levenstein et al.[34]; Figures 8B and S8A), which were used to select model parameters that best matched the data (Figure S8A). These duration statistics emerge because both populations spend their time in complementary excitable states (low-rate iSWR in HPC; high-rate UP in RSC; Figure 8C). In the HPC, noise can cause a transition to a transiently stable high-rate SWR state, which is subsequently destabilized by the effect of adaptation (Figure 8C, red shading). In the RSC, noise can cause a transition to a transiently stable DOWN state, which is subsequently destabilized by the effect of I_h (Figure 8C, gray shading).

In addition to each region's local connectivity, we coupled the RSC and HPC using excitatory projections that targeted the excitatory and inhibitory populations in the partner region (Figure 8A; STAR Methods). This coupled network exhibited increased incidence of SWRs prior to DOWN states (Figure 8E, compare with Figures 4D and 4E), decreased hippocampal population rate and SWR probability (pSWR) during cortical DOWN states (Figure 8D, compare with Figure 3), and increased SWR probability following cortical DOWN-UP transitions (Figure 8E, compare with Figures 4D and 4E), as in our experimental findings. Analysis of the phase planes revealed that these temporal relationships emerged because the influence of each region on the other modulates the stability of fixed points, and thus the probability of transitions, at critical times (Figure 8F; Video S6). During a SWR, increased drive from the HPC decreases the stability of the RSC UP state, increasing the probability of a U-D transition (Figure 8Fi). During the DOWN state, lower drive from the RSC decreases the HPC firing rate during the hippocampal iSWR and increases its stability, decreasing the probability of an iSWR → SWR transition (Figure 8Fii). Following the DOWN state, I_h transiently increases the firing rate of the RSC UP state fixed point, which provides increased drive to the HPC, thus decreasing the stability of the hippocampal iSWR state and increasing pSWR (Figure 8Fiii).

Further analysis of the model revealed two additional insights. First, the ability of SWRs to evoke a cortical DOWN state relied primarily on the influence of hippocampal activity on cortical interneurons (Figure S8B), as has been observed experimentally

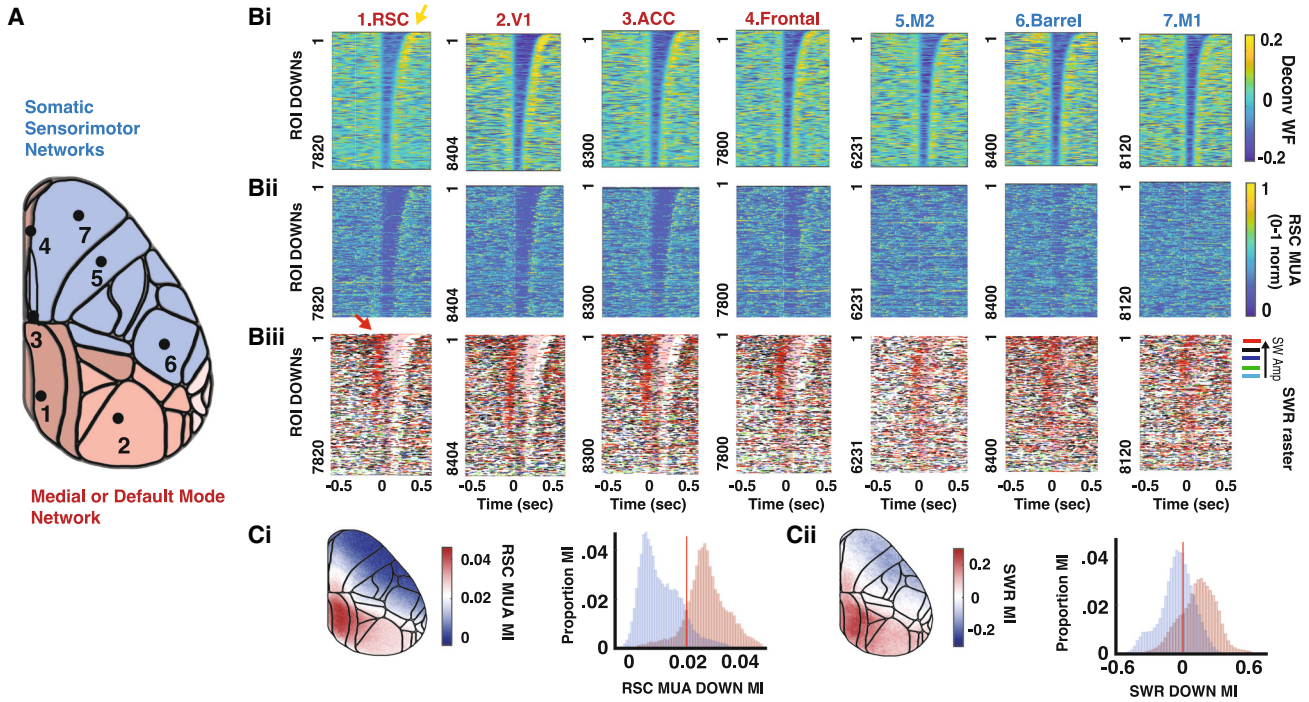

Figure 6. Probability of SWRs surrounding DOWN states across dorsal neocortex

(A) Map of regions visible in imaging field of view (FOV), color-coded by membership in medial network (red) or somatic sensorimotor networks (blue), as in Zingg et al.[44] Numbered regions correspond to columns in (Bi)–(Biii).

(Bi) Deconvolved wide-field activity surrounding wide-field-detected DOWN states in the region specified (25th percentile of pixel WF values and below = DOWN state), as described in Figure S8 and STAR Methods. Sorted by duration DOWN for an example mouse, separately in each region.

(Bii) RSC MUA surrounding the same DOWN states for each region.

(Biii) Raster plot of SWRs surrounding the same DOWN states, color-coded by SWR amplitude quintiles (small to large: green, cyan, blue, black, and red). Note that large-amplitude SWRs (red) precede U-D transitions for long DOWN states, red arrow.

(Ci) Average modulation index (MI; see STAR Methods) of RSC MUA by DOWN states detected across all pixels and all mice; positive MI corresponds to higher RSC MUA during UP than DOWN for the given pixel (see STAR Methods for details); left, MI plotted on dorsal map, right, distribution of same values separated by medial (red) and sensorimotor networks (blue).

(Cii) Average modulation of SWRs relative to DOWN states across all regions; left, MI plotted on dorsal map, right, distribution of same values separated by medial (red) and sensorimotor networks (blue).

with hippocampo-cortical[65,66] and cortico-cortical[67] projections. Second, the temporal relationships observed between SWRs and DOWN states relied directly on bi-directional interaction between the HPC and RSC, as a "lesion" of RSC → HPC projections resulted in a loss of DOWN-state modulation of hippocampal MUA and thus modulation of pSWR (Figure S8C). Conversely, lesion of the HPC → RSC projection removed the increased probability of SWRs at U-D and D-U transitions (Figure S8D). Together, these results indicate that a mechanism involving coupled excitable systems is sufficient to explain the putative state-dependent, bi-directional interaction observed between the HPC and RSC.

DISCUSSION

Using a combination of wide-field imaging of mouse dorsal neocortex and electrophysiological recordings from the RSC and HPC, we found evidence of a topographically confined, bi-directional interaction between the HPC and neocortex that varied in strength, with ultraslow fluctuations in arousal level. In addition to the modulation of SWR rate by UP/DOWN states in the DMN, population-level state transitions in one structure had a precise temporal relationship with state transitions in the other. From the cortex to HPC, SWRs followed rebound excitation at D-U transitions, or K-complexes, in the DMN, with a characteristic latency. From the HPC to the cortex, large-amplitude SWRs were followed by an increased probability of DOWN states in the RSC and antero-lateral motor areas, which spread following cortico-cortical connectivity. A model of weakly coupled excitable systems accounted for the major experimental observations.

Putative bi-directional hippocampal-neocortical interaction

Our findings support and extend previous work suggesting a hippocampal-neocortical "dialog" during NREM sleep. Previous electrophysiological experiments often recorded from the HPC and a single partner region. As a result, mechanistic hypotheses proposed based on the observed temporal relationships varied, including that SWRs trigger either UP states or DOWN states or

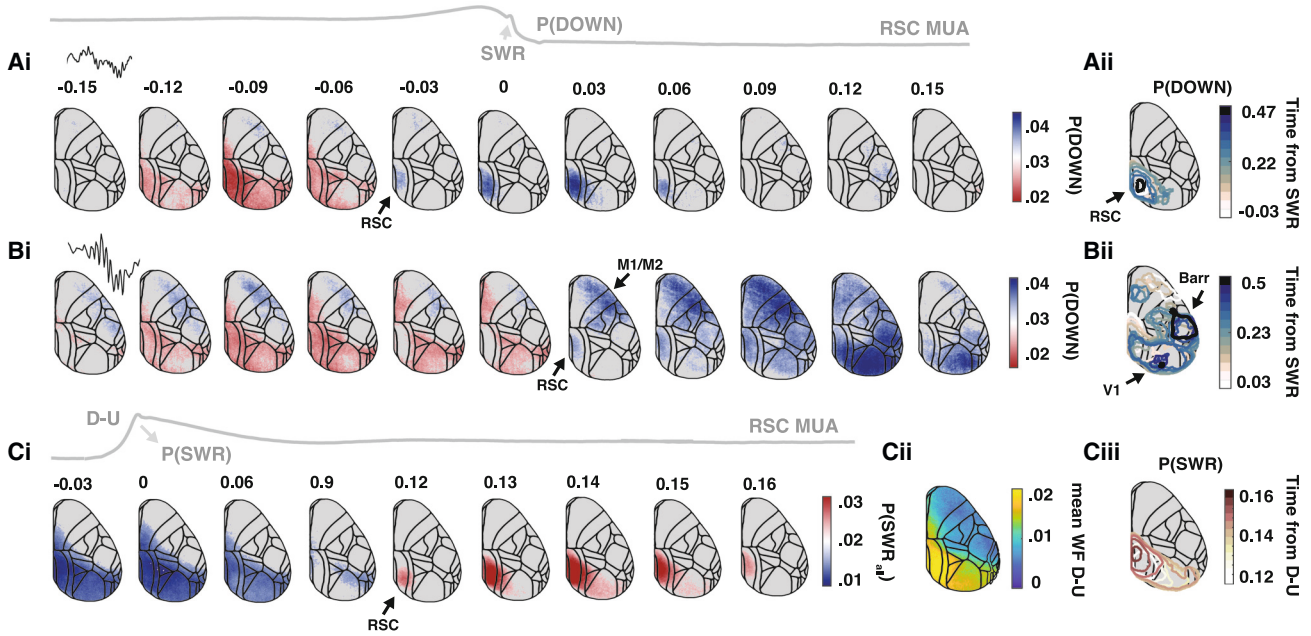

Figure 7. Average topography of putative interaction between hippocampal SWRs and neocortical DOWN states

(Ai) Average probability of DOWN state occurrence across all pixels aligned to low amplitude SWRs (amplitude quintile 1 of 5; t = 0, peak of SWRs). Colored portion of plots denotes the time points at which the given pixel is above (blue) or below (red) a 95th percentile bootstrapped confidence interval, obtained by shuffling SWR peak times across all SWRs and re-computing cross correlograms (n = 500).

(Aii) Outline of DOWN states from the onset of DOWN in RSC (white outline) to a sink in RSC (dark blue outline), colored by latency with respect to SWR peak.

(Bi) Same as (Ai) but for SWR amplitude quintile 5 of 5. Note onset of DOWN states 30 ms following SWR peak in both RSC and regions across sensorimotor network.

(Bii) Outline of DOWN states from onset of DOWN in RSC and sensorimotor regions (white outlines) to sinks in V1 and barrel cortex (dark blue outlines), colored by latency with respect to SWR peak.

(Ci) The probability of SWR occurrence aligned to D-U transitions (t = 0) for every pixel. Colored portion of plots denotes the time points at which the given pixel is above (blue) or below (red) a 95th percentile bootstrapped confidence interval, computed as in (Ai) and (Bi) but with shuffled D-U transition times.

(Cii) Mean wide-field activity within 20 ms of the D-U transition for each pixel.

(Ciii) Outline of significant increase in P(SWR) following D-U transitions for successive frames.

that the neocortex primes the spike content of SWRs.[8–16,68] Recent imaging experiments attempted to address these contradictions by considering regional variation in coupling, but these either lacked the temporal resolution needed to resolve direction of interaction, did not record during NREM sleep, or arrived at hypotheses that differ from ours.[31–33]

From the neocortex to the HPC

Our experiments show that hippocampal spiking activity tracks UP/DOWN states in neocortical regions restricted to mouse DMN, with the most pronounced co-variation between the RSC and HPC during deep NREM. Previously referred to as "frames" of co-activity,[9,10] this co-variation may be enabled by a common third-party drive, for example, from subcortical sources.[69,70] Another possibility is that the traveling UP/DOWN states characteristic of NREM sleep spread to the RSC or entorhinal cortex, monosynaptic partners of HPC, which in turn directly drive hippocampal circuits. In support of the latter, in our model, increased input to the HPC during cortical UP states increases the excitability of the HPC. This caused an increase in both HPC population rate and SWR rate due to an increase in the ease with which noise or external perturbation can "kick" HPC into a SWR state. In support of this scenario, it was previously reported that both the firing rates of hippocampal neurons and SWR incidence decrease during bilateral optogenetic silencing of the medial entorhinal cortex.[13] The excitability of hippocampal and cortical populations has also been demonstrated to increase with deepening NREM,[34] which is reflected in the increased modulation of HPC by RSC UP/DOWN states with deepening sleep.

In addition to the modulation of hippocampal excitability by UP/DOWN states and NREM depth, a disproportionate number of SWRs occurred following DMN D-U transitions at a fixed lag (SWR_{DU}). The putative trigger for SWR_{DU} is the rebound excitation following D-U transitions, known as the K-complex in scalp electroencephalogram (EEG) recordings. Our model supports our interpretation of these observations. In the model, D-U-induced K-complexes occur because activation of the h-current during RSC DOWN states results in transient rebound excitation at the D-U transition prior to settling into an UP state. This D-U "rebound excitation" destabilizes the iSWR state in the HPC population, thus increasing the probability of SWR occurrence.

Of note, the increase in HPC excitability lagged behind the onset of UP states in the RSC and other DMN regions. Mirroring this, SWR_{DU} did not occur in tandem with K-complexes but

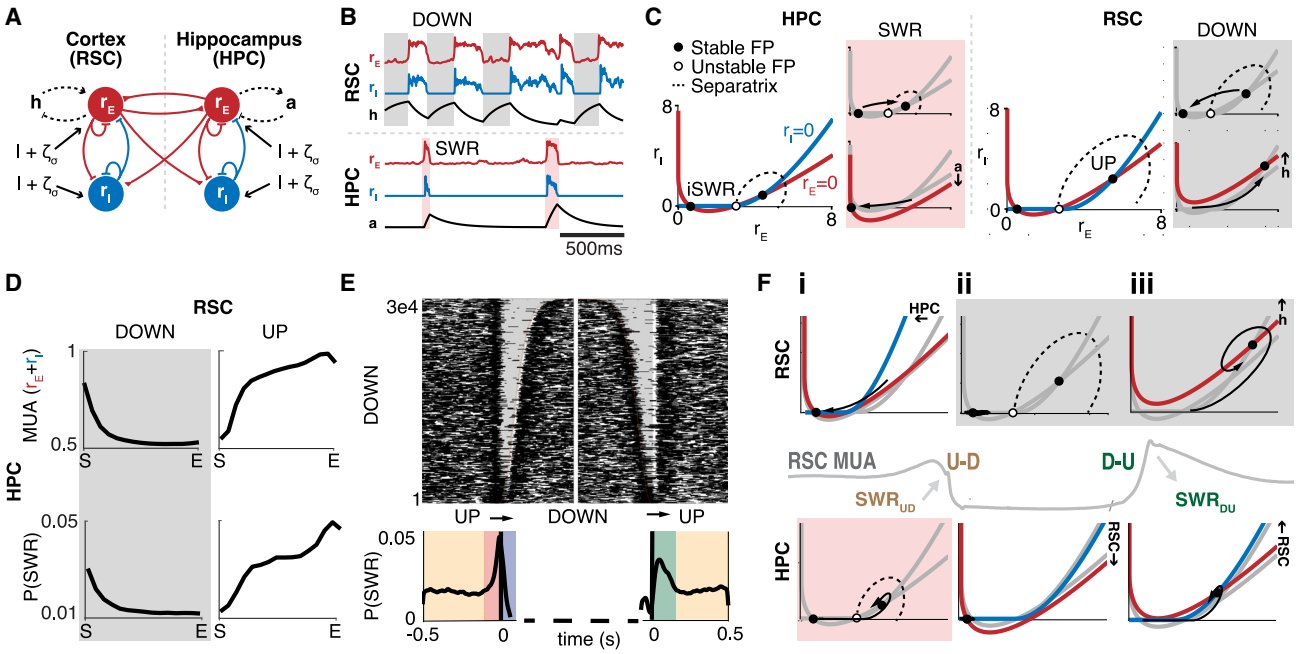

Figure 8. Model of the bi-directional interactions between HPC and RSC

(A) Two-region firing rate model of HPC and RSC, with long-range projections between the two regions. Each region comprises of recurrently connected excitatory (E) and inhibitory (I) populations with independent background noise. The E populations are subject to a slow feedback current (h-current [h] in RSC, adaptation [a] in HPC, see STAR Methods).

(B) Model simulation outputs for E and I populations in the two regions and feedback currents.

(C) I-E phase planes for RSC and HPC. Both regions show two stable steady states (a DOWN and an UP state for RSC and an iSWR and a SWR state for HPC). The basin of attraction for each steady state is bounded by a separatrix passing through an unstable fixed point (FP). In the HPC (left), a transition from the iSWR to the SWR state engages the adaptative current, which destabilizes the SWR state. In the cortex (right), a transition from the UP to the DOWN state engages the h-current, which destabilizes the DOWN state.

(D) From top to bottom: HPC MUA and P(SWR) plotted as a function of time-normalized RSC UP and preceding DOWN states (compare with Figure 3).

(E) Top, raster plot of all SWRs surrounding the DOWN state. Note as in experimental data, clustering of SWRs around UP and DOWN state transitions. Bottom, P(SWR) surrounding state transitions reveals a peak before the U-D transition and after the D-U transition (compare with Figure 4).

(F) Analysis of the phase planes for SWR-UP/DOWN interaction. (i, SWR_{UD}) Increased hippocampal activity in the SWR state displaces the RSC nullclines, destabilizing the UP state fixed point and pushing the trajectory to a DOWN state. (ii) Low RSC activity in the DOWN state lowers the HPC E nullcline, reducing the P(SWR). (iii, SWR_{DU}) Activation of the h-current during the DOWN state results in increased RSC activity following the D-U transition. High RSC activity displaces the HPC nullclines, destabilizing the iSWR fixed point and pushing the trajectory to a SWR.

rather followed D-U transitions in RSC with a delay of 120 ms (Video S5B). An explanation for this delay is not readily captured by our model, even with delayed differential equations (see STAR Methods). It is possible that the excitatory drive from the RSC is not direct and occurs primarily via a polysynaptic pathway through either the entorhinal cortex or thalamus.[13,71] However, a similarly long delay has been observed between entorhinal cortical D-U transitions and SWRs.[9] An alternative possibility is that excitatory input drives dentate granule cells, which exert a transient inhibitory effect on CA3 pyramidal cells, via feed-forward inhibition,[9,15,72] and that the release of those CA3 pyramidal cells from hyperpolarization induces synchronous rebound spiking.[73,74] Multi-site recordings in the RSC, entorhinal cortex, HPC, and thalamus, or brief optogenetic hyperpolarization of CA3 neurons, will be needed to test these hypotheses.

From the HPC to the neocortex

In the reverse direction, as SWR amplitude and depth of sleep increased, the probability of retrosplenial cortical DOWN states following SWRs at a fixed lag also increased (SWR_{UD}).[12,19,75] This temporal relationship is not without precedence, as in humans DOWN states often follow SWRs[76] and interictal epileptiform events in the HPC reliably induce DOWN states in both humans and rodents.[7] Our model suggests a mechanism by which SWR-induced DOWN states could occur. A SWR transiently destabilizes the UP state via a strong drive of the local cortical inhibitory population, resulting in increased probability of transition to a DOWN state. Deepening NREM sleep further destabilizes DOWN states,[34] contributing to this effect. This mechanism is corroborated by a recent paper that optogenetically stimulated hippocampal terminals in the RSC and found an increase in the firing rate of inhibitory, but not excitatory, cells, followed by a DOWN state.[66] In our wide-field data, we further observed that sufficiently large-amplitude SWRs were followed by DOWN states in the RSC or anterolateral motor regions that then spread across much of the neocortex, with average sinks in the barrel and primary visual cortical regions. This may be facilitated by cortico-cortical or thalamo-cortical projections. For example, the RSC is a "hub" in the

DMN[36,77] and shares dense bi-directional projections with regions across the visual hierarchy. SWR_{UD} could ultimately lead to a DOWN state in V1 via induction of a DOWN state in the RSC that then propagates along hierarchically connected visual areas. Alternatively, DOWN state induction in early sensory areas could happen via thalamo-cortical disfacilitation, supported by the observation that numerous thalamic nuclei are silenced during SWRs[19,23,78] and the larger the amplitude SWR, the more global it is along the longitudinal axis of the HPC.[19] Overall, these observations suggest that SWR_{UD} events exert an influence on neocortical activity proportional to SWR amplitude that then propagates across neocortex.

An unexpected observation, in light of previous claims,[14,17,18] was the absence of SWRs preceding and thus putatively inducing UP states. We observed only a small fraction of SWRs during DOWN states, often timed by the K-complex of a preceding short-duration UP state at ~120 ms. The failure of SWR_D to induce a D-U transition could be explained by their low probability, low amplitude, or refractoriness of the target circuits. In line with this latter explanation, SWRs during DOWN states evoked EPSPs in entorhinal neurons but failed to discharge them,[9] preventing the propagation of excitation. We also note that there were more U-D and D-U transitions than SWR_{UD} and SWR_{DU} events, implying that only a fraction of these transitions were induced by (or induced) a SWR. One possible explanation for this is that traveling slow oscillations[26] observed in the DMN or RSC may fail to invade the entorhinal cortex, the primary input to the HPC. Another explanation, afforded by our model, is that both regions are only weakly coupled and thus capable of noise-driven transitions independently of one another. Further, our experimental studies examined these interactions in "spontaneous" states, but we expect that these interactions will be biased by prior learning or emotional experience.

Putative functions of SWR types

The ability to distinguish SWRs by their timing with respect to neocortical UP and DOWN transitions could help disentangle the direction of spike transmission between the HPC and neocortex and thus the mechanistic contribution of these "SWR types" to memory. One possibility is that the observed SWR types support distinct functions, such as encoding, consolidation, or priming of recalled events. In a recent study, hippocampal reactivation occurred during prefrontal cortical UP states, whereas the strongest coordination between the RSC and HPC occurred during U-D transitions in the RSC.[79] SWR_D events, some of which may be triggered by K-complexes, can sporadically activate a few neocortical pyramidal cells during the DOWN state. This sporadic spiking during DOWN states has been suggested to be the critical driver of consolidation of recently acquired experience.[80] However, this explanation alone would leave the function of the great majority of SWRs unexplained, other than serving subcortical, autonomic functions.[81] In contrast, another study emphasized the importance of distinct, brain-wide coordinated and uncoordinated SWR events during UP states.[82]

A complementary hypothesis is that the four types of SWRs are better understood as part of a multi-regional "dynamical motif" enabling systems consolidation,[83] facilitated by the excitable regimes characteristic of NREM sleep.[34] SWRs, if sufficiently large, may induce a DOWN state (SWR_{UD}). This DOWN state may invade the thalamus, inducing a thalamo-cortical spindle,[84] and the rebound excitation from the D-U transition may then initiate a SWR burst (SWR_{DU} and SWR_U) in the HPC that is coordinated with that induced spindle. In support of this, memory reactivations in humans occur when SWRs are coupled to slow oscillations and spindles but not during solitary slow oscillations or spindles.[85] Further, SWR bursts are likely important for consolidation in light of reports that long-duration neuronal spike sequences, reflecting long trajectories in a previously experienced environment, span several hundred milliseconds, and often abridge two or more SWR events occurring in a burst.[86] Whereas SWR_{DU} are more likely to reflect burst onsets, SWR_{UD} may play a role in ending both a SWR burst in the HPC and an UP state in neocortex. One can speculate that the ensuing silence serves as the truncation of coordinated exploration along a given attractor or the expression of a memory trace, allowing exploration of the next.[24]

Arousal levels affect interregional perturbation

Ultraslow and infraslow fluctuations in arousal level have long been observed in both humans and rodents.[20] However, the link between these slow timescale changes and fast timescale hippocampal-neocortical interaction has remained elusive, resulting in largely separate rodent and human literatures. We suggest that the dynamical regime, and thus excitability, of brain circuits fluctuates across ultraslow and infraslow timescales, likely due to the slow changes in neuromodulatory tone accompanying transitions in arousal level.[87,88] Ultraslow fluctuations may reflect global changes in arousal level, whereas infraslow fluctuations may reflect changes in regime within resting state networks. Given the hypothesized fluctuations in regime, these slow rhythms reflect the propensity with which the regions belonging to the given resting state network can be perturbed.[34] For example, an "active" DMN corresponds to an increased rate of SWRs and DOWN states in DMN regions,[27] which arise due to the more excitable regime the DMN is in, facilitating interregional communication within, but not across, resting state networks. Finally, SWR types arise because of the transition from less to more excitable regimes over the course of deepening sleep. If sufficiently excitable, or if the perturbation is sufficiently large, SWRs (SWR_{UD}) can cause DOWN states and D-U transitions can cause SWRs (SWR_{DU}). These perturbations can then propagate as a function of the state and anatomical connectivity of the downstream structure. This provides a mechanism by which SWR perturbation can propagate along the neocortical hierarchy, mediated by sleep depth.

We did not distinguish explicitly between wake and sleep SWRs. This may be considered a caveat, given the distinct functions they are often assigned.[87,89,90] However, our observations and previous results[91] do not support a clear delineation between wake and sleep but rather a transition toward an increasingly excitable neural regime as an animal moves through quiet wake to deep NREM sleep states. Supporting this notion, UP-DOWN states are present during quiet wake but are notably more localized, as is the impact of perturbation via SWRs.[15,91–95]

Further experiments are needed to reveal whether waking and NREM SWRs are qualitatively different in their interaction with the neocortex or whether they are better understood as existing along a continuum.

RESOURCE AVAILABILITY

Lead contact

Requests for further information and resources should be directed to and will be fulfilled by the lead contact, Gyorgy Buzsáki.

Materials availability

This study did not generate new unique reagents.

Data and code availability

A subset of the data that support the findings of this study will be made available on the Buzsáki lab website (https://buzsakilab.com/wp/resources/), and all data will be made available upon reasonable request. The code used for this study was adapted from the buzcode repository (https://github.com/buzsakilab/buzcode).

ACKNOWLEDGMENTS

The authors thank members of the Basu and Buzsáki labs for support and feedback. This work was supported by NIH grants MH122391, MH 139216 (G.B. and J.B.), U19 NS107616 (G.B.), R01 NS109362 (J.B.), R01 NS109994 (J.B.), R01MH062346 (X.-J.W.), and R90DA060339 (E.C.).

AUTHOR CONTRIBUTIONS

R.A.S., G.B., and J.B. designed the research. R.A.S., N.M., and M.V. performed the research. R.A.S. analyzed the data. E.C. modeled the data, guided by R.A.S., D.L., and X.-J.W. R.A.S., G.B., and J.B. wrote the paper, with the contribution of all authors.

DECLARATION OF INTERESTS

The authors declare no competing interests.

STAR★METHODS

Detailed methods are provided in the online version of this paper and include the following:

- KEY RESOURCES TABLE
- METHOD DETAILS
  - Animal handling
  - Surgical procedures
  - Behavior
  - Electrophysiological Recordings
  - Widefield Recordings
  - Histology
- DATA ANALYSIS
  - Electrophysiological data preprocessing
  - Widefield data preprocessing
  - Multiple unit activity (MUA) extraction
  - UP/DOWN state detection
  - Ripple detection and analysis
  - Tonic MUA
  - Average variables across time normalized UP/DOWN states
  - Brain State Scoring
  - PSS Power spectrum slope (PSS)
  - Computing SWR phase-relationship with infraslow blood flow signal
  - Spectrograms x infraslow phase
  - Identification of SWR types
  - Calculation of DOWN states in widefield data
  - DOWN state modulation index
  - Cross-correlograms of widefield data
  - Computing cross-correlograms to test whether the strength of input impacts population-level state transition in downstream region
  - Testing the effect of input strength and state of downstream region on probability of evoking a population-level state transition via repeated measures ANOVA
  - Predicting duration DOWN state or magnitude of sharp wave using input strength and local state as predictors in a generalized linear model
  - Statistical methods
- MODEL SETUP
  - Model implementation
  - Local Connection Strengths
  - Long Range Connection Strengths
  - Model Parameters

SUPPLEMENTAL INFORMATION

Supplemental information can be found online at https://doi.org/10.1016/j.neuron.2024.12.019.

Received: March 15, 2024
Revised: October 26, 2024
Accepted: December 18, 2024
Published: January 27, 2025

REFERENCES

1. McClelland, J.L., McNaughton, B.L., and O'Reilly, R.C. (1995). Why there are complementary learning systems in the hippocampus and neocortex: insights from the successes and failures of connectionist models of learning and memory. Psychol. Rev. *102*, 419–457. https://doi.org/10.1037/0033-295X.102.3.419.
2. Kumaran, D., Hassabis, D., and McClelland, J.L. (2016). What Learning Systems do Intelligent Agents Need? Complementary Learning Systems Theory Updated. Trends Cogn. Sci. *20*, 512–534. https://doi.org/10.1016/j.tics.2016.05.004.
3. Alvarez, P., and Squire, L.R. (1994). Memory consolidation and the medial temporal lobe: A simple network model. Proc. Natl. Acad. Sci. USA *91*, 7041–7045. https://doi.org/10.1073/pnas.91.15.7041.
4. Buzsáki, G. (2015). Hippocampal sharp wave-ripple: A cognitive biomarker for episodic memory and planning. Hippocampus *25*, 1073–1188.
5. Wittkuhn, L., Chien, S., Hall-McMaster, S., and Schuck, N.W. (2021). Replay in minds and machines. Neurosci. Biobehav. Rev. *129*, 367–388. https://doi.org/10.1016/j.neubiorev.2021.08.002.
6. Maingret, N., Girardeau, G., Todorova, R., Goutierre, M., and Zugaro, M. (2016). Hippocampo-cortical coupling mediates memory consolidation during sleep. Nat. Neurosci. *19*, 959–964.
7. Gelinas, J.N., Khodagholy, D., Thesen, T., Devinsky, O., and Buzsáki, G. (2016). Interictal epileptiform discharges induce hippocampal-cortical coupling in temporal lobe epilepsy. Nat. Med. *22*, 641–648.
8. Bendor, D., and Wilson, M.A. (2012). Biasing the content of hippocampal replay during sleep. Nat. Neurosci. *15*, 1439–1444.
9. Isomura, Y., Sirota, A., Ozen, S., Montgomery, S., Mizuseki, K., Henze, D.A., and Buzsáki, G. (2006). Integration and Segregation of Activity in Entorhinal-Hippocampal Subregions by Neocortical Slow Oscillations. Neuron *52*, 871–882.
10. Ji, D., and Wilson, M.A. (2007). Coordinated memory replay in the visual cortex and hippocampus during sleep. Nat. Neurosci. *10*, 100–107.
11. Peyrache, A., Khamassi, M., Benchenane, K., Wiener, S.I., and Battaglia, F.P. (2009). Replay of rule-learning related neural patterns in the prefrontal cortex during sleep. Nat. Neurosci. *12*, 919–926.

12. Sirota, A., Csicsvari, J., Buhl, D., and Buzsáki, G. (2003). Communication between neocortex and hippocampus during sleep in rodents. Proc. Natl. Acad. Sci. USA *100*, 2065–2069.

13. Zutshi, I., and Buzsáki, G. (2023). Hippocampal sharp-wave ripples and their spike assembly content are regulated by the medial entorhinal cortex II II Article Hippocampal sharp-wave ripples and their spike assembly content are regulated by the medial entorhinal cortex. Curr. Biol. *33*, 3648–3659.e4.

14. Battaglia, F.P., Sutherland, G.R., and Mcnaughton, B.L. (2004). Hippocampal sharp wave bursts coincide with neocortical "up-state" transitions. Learn. Mem. *11*, 697–704.

15. Kajikawa, K., Hulse, B.K., Siapas, A.G., and Lubenov, E.V. (2022). UP-DOWN states and ripples differentially modulate membrane potential dynamics across DG, CA3 , and CA1 in awake mice. eLife *11*, e69596.

16. Mölle, M., Eschenko, O., Gais, S., Sara, S.J., and Born, J. (2009). The influence of learning on sleep slow oscillations and associated spindles and ripples in humans and rats. Eur. J. Neurosci. *29*, 1071–1081.

17. Jadhav, S.P., Kemere, C., German, P.W., and Frank, L.M. (2012). Awake hippocampal sharp-wave ripples support spatial memory. Science *336*, 1454–1458.

18. Sanda, P., Malerba, P., Jiang, X., Krishnan, G.P., Gonzalez-Martinez, J., Halgren, E., and Bazhenov, M. (2021). Bidirectional Interaction of Hippocampal Ripples and Cortical Slow Waves Leads to Coordinated Spiking Activity during NREM Sleep. Cereb. Cortex *31*, 324–340.

19. Nitzan, N., Swanson, R., Schmitz, D., and Buzsáki, G. (2022). Brain-wide interactions during hippocampal sharp wave ripples. Proc. Natl. Acad. Sci. USA *119*, e2200931119.

20. Watson, B.O., Levenstein, D., Greene, J.P., Gelinas, J.N., and Buzsáki, G. (2016). Network Homeostasis and State Dynamics of Neocortical Sleep. Neuron *90*, 839–852.

21. Genzel, L., Kroes, M.C.W., Dresler, M., and Battaglia, F.P. (2014). Light sleep versus slow wave sleep in memory consolidation: a question of global versus local processes? Trends Neurosci. *37*, 10–19.

22. Siapas, A.G., and Wilson, M.A. (1998). Coordinated Interactions between Hippocampal Ripples and Cortical Spindles during Slow-Wave Sleep of SWS and during behavioral immobility. Neuron *21*, 1123–1128.

23. Logothetis, N.K., Eschenko, O., Murayama, Y., Augath, M., Steudel, T., Evrard, H.C., Besserve, M., and Oeltermann, A. (2012). Hippocampal-cortical interaction during periods of subcortical silence. Nature *491*, 547–553.

24. Pazienti, A., Galluzzi, A., Dasilva, M., Sanchez-Vives, M.V., and Mattia, M. (2022). Slow waves form expanding , memory-rich mesostates steered by local excitability in fading anesthesia. iScience *25*, 103918. https://doi.org/10.1101/2021.01.21.427671.

25. Massimini, M., Huber, R., Ferrarelli, F., Hill, S., and Tononi, G. (2004). The Sleep Slow Oscillation as a Traveling Wave. J. Neurosci. *24*, 6862–6870.

26. Mohajerani, M.H., Chan, A.W., Mohsenvand, M., LeDue, J., Liu, R., McVea, D.A., Boyd, J.D., Wang, Y.T., Reimers, M., and Murphy, T.H. (2013). Spontaneous cortical activity alternates between motifs defined by regional axonal projections. Nat. Neurosci. *16*, 1426–1435.

27. Kaplan, R., Adhikari, M.H., Hindriks, R., Mantini, D., Murayama, Y., Logothetis, N.K., and Deco, G. (2016). Hippocampal Sharp-Wave Ripples Influence Selective Activation of the Default Mode Network. Curr. Biol. *26*, 686–691. https://doi.org/10.1016/j.cub.2016.01.017.

28. Higgins, C., Liu, Y., Vidaurre, D., Kurth-Nelson, Z., Dolan, R., Behrens, T., and Woolrich, M. (2021). Replay bursts in humans coincide with activation of the default mode and parietal alpha networks. Neuron *109*, 882–893.e7. https://doi.org/10.1016/j.neuron.2020.12.007.

29. Raichle, M.E. (2015). The brain's default mode network. Annu. Rev. Neurosci. *38*, 433–447.

30. Gu, S., Pasqualetti, F., Cieslak, M., Telesford, Q.K., Yu, A.B., Kahn, A.E., Medaglia, J.D., Vettel, J.M., Miller, M.B., Grafton, S.T., et al. (2015). Controllability of structural brain networks. Nat. Commun. *6*, 8414. https://doi.org/10.1038/ncomms9414.

31. Karimi Abadchi, J., Nazari-Ahangarkolaee, M., Gattas, S., Bermudez-Contreras, E., Luczak, A., McNaughton, B.L., and Mohajerani, M.H. (2020). Spatiotemporal patterns of neocortical activity around hippocampal sharp-wave ripples. eLife *9*, e51972.

32. Abadchi, J.K., Rezaei, Z., Knöpfel, T., Mcnaughton, B.L., and Mohajerani, M.H. (2023). Inhibition is a prevalent mode of activity in the neocortex around awake hippocampal ripples in mice. eLife *12*, 1–22.

33. Pedrosa, R., Nazari, M., Mohajerani, M.H., Knöpfel, T., Stella, F., and Battaglia, F.P. (2022). Hippocampal gamma and sharp wave/ripples mediate bidirectional interactions with cortical networks during sleep. Proc. Natl. Acad. Sci. USA *119*, e2204959119.

34. Levenstein, D., Buzsáki, G., and Rinzel, J. (2019). NREM sleep in the rodent neocortex and hippocampus reflects excitable dynamics. Nat. Commun. *10*, 2478.

35. Lee, J.H., Kim, W.B., Park, E.H., and Cho, J.H. (2023). Neocortical synaptic engrams for remote contextual memories. Nat. Neurosci. *26*, 259–273. https://doi.org/10.1038/s41593-022-01223-1.

36. Alexander, A.S., Place, R., Starrett, M.J., Chrastil, E.R., and Nitz, D.A. (2023). Rethinking retrosplenial cortex: Perspectives and predictions. Neuron *111*, 150–175. https://doi.org/10.1016/j.neuron.2022.11.006.

37. Cowansage, K.K., Shuman, T., Dillingham, B.C., Chang, A., Golshani, P., and Mayford, M. (2014). Direct Reactivation of a Coherent Neocortical Memory of Context. Neuron *84*, 432–441. https://doi.org/10.1016/j.neuron.2014.09.022.

38. Milczarek, M.M., Vann, S.D., and Sengpiel, F. (2018). Spatial Memory Engram in the Mouse Retrosplenial Cortex. Curr. Biol. *28*, 1975–1980.e6. https://doi.org/10.1016/j.cub.2018.05.002.

39. De Sousa, A.F., Cowansage, K.K., Zutshi, I., Cardozo, L.M., Yoo, E.J., Leutgeb, S., and Mayford, M. (2019). Optogenetic reactivation of memory ensembles in the retrosplenial cortex induces systems consolidation. Proc. Natl. Acad. Sci. USA *116*, 8576–8581. https://doi.org/10.1073/pnas.1818432116.

40. Dana, H., Chen, T.-W., Hu, A., Shields, B.C., Guo, C., Looger, L.L., Kim, D.S., and Svoboda, K. (2014). Thy1-GCaMP6 Transgenic Mice for Neuronal Population Imaging In Vivo. PLoS One *9*, e108697.

41. Ma, Y., Shaik, M., Kim, S., Kozberg, M., Zhao, H., Yu, H., and Hillman, E. (2016). High-speed, wide-field optical mapping (WFOM) of neural activity and brain haemodynamics: Considerations and novel approaches. Philos. Trans. R. Soc. Lond. B Biol. Sci. *371*, 20150360.

42. Wang, Q., Ding, S.-L., Li, Y., Royall, J., Feng, D., Lesnar, P., Graddis, N., Naeemi, M., Facer, B., Ho, A., et al. (2020). The Allen Mouse Brain Common Coordinate Framework: A 3D Reference Atlas. Cell *181*, 936–953.e20. https://doi.org/10.1016/j.cell.2020.04.007.

43. Peters, A.J., Fabre, J.M.J., Steinmetz, N.A., Harris, K.D., and Carandini, M. (2021). Striatal activity topographically reflects cortical activity. Nature *591*, 420–425.

44. Zingg, B., Hintiryan, H., Gou, L., Song, M.Y., Bay, M., Bienkowski, M.S., Foster, N.N., Yamashita, S., Bowman, I., Toga, A.W., et al. (2014). Neural networks of the mouse neocortex. Cell *156*, 1096–1111. https://doi.org/10.1016/j.cell.2014.02.023.

45. Gao, R., Peterson, E.J., and Voytek, B. (2017). Inferring synaptic excitation/inhibition balance from field potentials. Neuroimage *158*, 70–78.

46. Levenstein, D., Gornet, J., Huszár, R., Girardeau, G., Grosmark, A., Peyrache, A., Senzai, Y., Watson, B.O., Mizuseki, K., Rinzel, J., et al. (2022). Distinct ground state and activated state modes of firing in forebrain neurons. Preprint at bioRxiv.

47. Lendner, J.D., Helfrich, R.F., Mander, B.A., Romundstad, L., Lin, J.J., Walker, M.P., Larsson, P.G., and Knight, R.T. (2020). An electrophysiological marker of arousal level in humans. eLife *9*, e55092. https://doi.org/10.7554/eLife.55092.

48. Vern, B.A., Schuette, W.H., Leheta, B., Juel, V.C., and Radulovacki, M. (1988). Low-frequency oscillations of cortical oxidative metabolism in waking and sleep. J. Cereb. Blood Flow Metab. *8*, 215–226.

49. Achermann, P., Dijk, D.J., Brunner, D.P., and Borbély, A.A. (1993). A model of human sleep homeostasis based on EEG slow-wave activity: Quantitative comparison of data and simulations. Brain Res. Bull. *31*, 97–113.

50. Lecci, S., Fernandez, L.M.J., Weber, F.D., Cardis, R., Chatton, J.Y., Born, J., and Lüthi, A. (2017). Coordinated infraslow neural and cardiac oscillations mark fragility and offline periods in mammalian sleep. Sci. Adv. *3*, e1602026. https://doi.org/10.1126/sciadv.1602026.

51. Yüzgeç, Ö., Prsa, M., Zimmermann, R., and Huber, D. (2018). Pupil Size Coupling to Cortical States Protects the Stability of Deep Sleep via Parasympathetic Modulation. Curr. Biol. *28*, 392–400.e3. https://doi.org/10.1016/j.cub.2017.12.049.

52. Watson, B.O. (2018). Cognitive and Physiologic Impacts of the Infraslow Oscillation. Front. Syst. Neurosci. *12*, 44. https://doi.org/10.3389/fnsys.2018.00044.

53. Mateo, C., Knutsen, P.M., Tsai, P.S., Shih, A.Y., and Kleinfeld, D. (2017). Entrainment of Arteriole Vasomotor Fluctuations by Neural Activity Is a Basis of Blood-Oxygenation-level-dependent "resting-state" connectivity. Neuron *96*, 936–948.e3.

54. Hiltunen, T., Kantola, J., Abou Elseoud, A.A., Lepola, P., Suominen, K., Starck, T., Nikkinen, J., Remes, J., Tervonen, O., Palva, S., et al. (2014). Infra-slow EEG fluctuations are correlated with resting-state network dynamics in fMRI. J. Neurosci. *34*, 356–362. https://doi.org/10.1523/JNEUROSCI.0276-13.2014.

55. Fox, M.D., and Raichle, M.E. (2007). Spontaneous fluctuations in brain activity observed with functional magnetic resonance imaging. Nat. Rev. Neurosci. *8*, 700–711. https://doi.org/10.1038/nrn2201.

56. Liu, T.T., Nalci, A., and Falahpour, M. (2017). The global signal in fMRI: Nuisance or Information? Neuroimage *150*, 213–229. https://doi.org/10.1016/j.neuroimage.2017.02.036.

57. Peyrache, A., Battaglia, F.P., and Destexhe, A. (2011). Inhibition recruitment in prefrontal cortex during sleep spindles and gating of hippocampal inputs. Proc. Natl. Acad. Sci. USA *108*, 17207–17212. https://doi.org/10.1073/pnas.1103612108.

58. Ahmadian, Y., Rubin, D.B., and Miller, K.D. (2013). Analysis of the Stabilized Supralinear Network. Neural Comput. *25*, 1994–2037. https://doi.org/10.1162/NECO_a_00472.

59. Jercog, D., Roxin, A., Barthó, P., Luczak, A., Compte, A., and De La Rocha, J. (2017). UP-DOWN cortical dynamics reflect state transitions in a bistable network. eLife *6*, e22425. https://doi.org/10.7554/eLife.22425.

60. Itskov, V., Curto, C., Pastalkova, E., and Buzsáki, G. (2011). Cell assembly sequences arising from spike threshold adaptation keep track of time in the hippocampus. J. Neurosci. *31*, 2828–2834. https://doi.org/10.1523/JNEUROSCI.3773-10.2011.

61. English, D.F., Peyrache, A., Stark, E., Roux, L., Vallentin, D., Long, M.A., and Buzsáki, G. (2014). Excitation and inhibition compete to control spiking during hippocampal ripples: Intracellular study in behaving mice. J. Neurosci. *34*, 16509–16517. https://doi.org/10.1523/JNEUROSCI.2600-14.2014.

62. Mehrotra, D., Levenstein, D., Duszkiewicz, A.J., Carrasco, S.S., Booker, S.A., Kwiatkowska, A., and Peyrache, A. (2024). Hyperpolarization-activated currents drive neuronal activation sequences in sleep. Curr. Biol. *34*, 3043–3054.e8. https://doi.org/10.1016/j.cub.2024.05.048.

63. Vesuna, S., Kauvar, I.V., Richman, E., Gore, F., Oskotsky, T., Sava-Segal, C., Luo, L., Malenka, R.C., Henderson, J.M., Nuyujukian, P., et al. (2020). Deep posteromedial cortical rhythm in dissociation. Nature *586*, 87–94. https://doi.org/10.1038/s41586-020-2731-9.

64. Robinson, R.B., and Siegelbaum, S.A. (2003). Hyperpolarization-activated cation currents: from molecules to physiological function. Annu. Rev. Physiol. *65*, 453–480. https://doi.org/10.1146/annurev.physiol.65.092101.142734.

65. Nitzan, N., Tukker, J.J., Mckenzie, S., Beed, P., and English, D.F. (2020). Propagation of hippocampal ripples to the neocortex by way of a subiculum-retrosplenial pathway. Nat. Commun. *11*, 1947.

66. Opalka, A.N., Huang, W.Q., Liu, J., Liang, H., and Wang, D.V. (2020). Hippocampal Ripple Coordinates Retrosplenial Inhibitory Neurons during Slow-Wave Sleep. Cell Rep. *30*, 432–441.e3. https://doi.org/10.1016/j.celrep.2019.12.038.

67. Ratliff, J.M., Terral, G., Lutzu, S., Heiss, J., Mota, J., Stith, B., Lechuga, A.V., Ramakrishnan, C., Fenno, L.E., Daigle, T., et al. (2024). Neocortical long-range inhibition promotes cortical synchrony and sleep. Preprint at bioRxiv. https://doi.org/10.1101/2024.06.20.599756.

68. Sullivan, D., Mizuseki, K., Sorgi, A., and Buzsáki, G. (2014). Comparison of sleep spindles and theta oscillations in the hippocampus. J. Neurosci. *34*, 662–674.

69. Narikiyo, K., Mizuguchi, R., Ajima, A., Shiozaki, M., Hamanaka, H., Johansen, J.P., Mori, K., and Yoshihara, Y. (2020). The claustrum coordinates cortical slow-wave activity. Nat. Neurosci. *23*, 741–753. https://doi.org/10.1038/s41593-020-0625-7.

70. Norimoto, H., Fenk, L.A., Li, H.H., Tosches, M.A., Gallego-Flores, T., Hain, D., Reiter, S., Kobayashi, R., Macias, A., Arends, A., et al. (2020). A claustrum in reptiles and its role in slow-wave sleep. Nature *578*, 413–418. https://doi.org/10.1038/s41586-020-1993-6.

71. Rhythms, H., Ngo, H.V., and Born, J. (2017). Thalamic Spindles Promote Memory Formation during Sleep through Triple Phase-Locking of Article Thalamic Spindles Promote Memory Formation during Sleep through Triple Phase-Locking of Cortical, Thalamic , and Hippocampal Rhythms. Neuron *95*, 424–435.e6. https://doi.org/10.1016/j.neuron.2017.06.025.

72. Acsády, L., Kamondi, A., Sík, A., Freund, T., and Buzsáki, G. (1998). GABAergic cells are the major postsynaptic targets of mossy fibers in the rat hippocampus. J. Neurosci. *18*, 3386–3403.

73. Stark, E., Roux, L., Eichler, R., Senzai, Y., Royer, S., and Buzsáki, G. (2014). Pyramidal cell-interneuron interactions underlie hippocampal ripple oscillations. Neuron *83*, 467–480.

74. Evangelista, R., Cano, G., Cooper, C., Schmitz, D., Maier, N., and Kempter, R. (2020). Generation of Sharp Wave-Ripple Events by Disinhibition. J. Neurosci. *40*, 7811–7836.

75. Inostroza, M., and Born, J. (2013). Sleep for preserving and transforming episodic memory. Annu. Rev. Neurosci. *36*, 79–102.

76. Staresina, B.P., Bergmann, T.O., Bonnefond, M., Meij, R. Van Der, Jensen, O., Deuker, L., Elger, C.E., Axmacher, N., and Fell, J. (2015). Hierarchical nesting of slow oscillations , spindles and ripples in the human hippocampus during sleep. Nat. Neurosci. *18*, 1679–1686.

77. Kaefer, K., Stella, F., McNaughton, B.L., and Battaglia, F.P. (2022). Replay, the default mode network and the cascaded memory systems model. Nat. Rev. Neurosci. *23*, 628–640.

78. Yang, M., Logothetis, N.K., and Eschenko, O. (2019). Occurrence of Hippocampal Ripples is Associated with Activity Suppression in the Mediodorsal Thalamic Nucleus. J. Neurosci. *39*, 434–444.

79. Feliciano-Ramos, P.A., Galazo, M., Penagos, H., and Wilson, M. (2023). Hippocampal memory reactivation during sleep is correlated with specific cortical states of the retrosplenial and prefrontal cortices. Learn. Mem. *30*, 221–236. https://doi.org/10.1101/lm.053834.123.

80. Todorova, R., and Zugaro, M. (2019). Isolated cortical computations during delta waves support memory consolidation. Science *366*, 377–381.

81. Tingley, D., McClain, K., Kaya, E., Carpenter, J., and Buzsáki, G. (2021). A metabolic function of the hippocampal sharp wave-ripple. Nature *597*, 82–86.

82. Shin, J.D., and Jadhav, S.P. (2024). Prefrontal cortical ripples mediate top-down suppression of hippocampal reactivation during sleep memory

consolidation. Curr. Biol. *34*, 2801–2811.e9. https://doi.org/10.1016/j.cub.2024.05.018.

83. Klinzing, J.G., Niethard, N., and Born, J. (2019). Mechanisms of systems memory consolidation during sleep. Nat. Neurosci. *22*, 1598–1610. https://doi.org/10.1038/s41593-019-0467-3.

84. Mak-McCully, R.A., Rolland, M., Sargsyan, A., Gonzalez, C., Magnin, M., Chauvel, P., Rey, M., Bastuji, H., and Halgren, E. (2017). Coordination of cortical and thalamic activity during non-REM sleep in humans. Nat. Commun. *8*, 15499. https://doi.org/10.1038/ncomms15499.

85. Schreiner, T., Petzka, M., Staudigl, T., and Staresina, B.P. (2021). Endogenous memory reactivation during sleep in humans is clocked by slow oscillation-spindle complexes. Nat. Commun. *12*, 3112.

86. Davidson, T.J., Kloosterman, F., and Wilson, M.A. (2009). Hippocampal replay of extended experience. Neuron *63*, 497–507.

87. Atherton, L.A., Dupret, D., and Mellor, J.R. (2015). Memory trace replay: the shaping of memory consolidation by neuromodulation. Trends Neurosci. *38*, 560–570.

88. Zhang, Y., Cao, L., Varga, V., Jing, M., Karadas, M., Li, Y., and Buzsáki, G. (2021). Cholinergic suppression of hippocampal sharp-wave ripples impairs working memory. Proc. Natl. Acad. Sci. USA *118*, e2016432118.

89. Foster, D.J., and Wilson, M.A. (2006). Reverse replay of behavioural sequences in hippocampal place cells during the awake state. Nature *440*, 680–683.

90. Berners-Lee, A., Feng, T., Silva, D., Wu, X., Ambrose, E.R., Pfeiffer, B.E., and Foster, D.J. (2022). Hippocampal replays appear after a single experience and incorporate greater detail with more experience. Neuron *110*, 1829–1842.e5.

91. Neske, G.T. (2015). The Slow Oscillation in Cortical and Thalamic Networks: Mechanisms and Functions. Front. Neural Circuits *9*, 88.

92. Osborne, J.E., and Dudman, J.T. (2014). RIVETS: A Mechanical System for In Vivo and In Vitro Electrophysiology and Imaging. PLoS One *9*, e89007.

93. Veraart, J., and Novikov, D.S. (2016). Denoising of diffusion MRI using random matrix theory Jelle. Neuroimage *142*, 394–406.

94. Afrashteh, N., Inayat, S., Mohsenvand, M., and Mohajerani, M.H. (2017). Optical-flow analysis toolbox for characterization of spatiotemporal dynamics in mesoscale optical imaging of brain activity. Neuroimage *153*, 58–74.

95. Tingley, D., and Buzsáki, G. (2020). Routing of Hippocampal Ripples to Subcortical Structures via the Lateral Septum. Neuron *105*, 138–149.e5.

96. Schomburg, E.W., Fernández-Ruiz, A., Mizuseki, K., Berényi, A., Anastassiou, C.A., Koch, C., and Buzsáki, G. (2014). Theta Phase Segregation of Input-Specific Gamma Patterns in Entorhinal-Hippocampal Networks. Neuron *84*, 470–485.

97. Pettersen, K.H., Devor, A., Ulbert, I., Dale, A.M., and Einevoll, G.T. (2006). Current-source density estimation based on inversion of electrostatic forward solution: Effects of finite extent of neuronal activity and conductivity discontinuities. J. Neurosci. Methods *154*, 116–133. https://doi.org/10.1016/j.jneumeth.2005.12.005.

98. Yamabe, M., Horie, K., Shiokawa, H., Funato, H., Yanagisawa, M., and Kitagawa, H. (2019). MC-SleepNet: Large-scale Sleep Stage Scoring in Mice by Deep Neural Networks. Sci. Rep. *9*, 15793.

99. Berens, P. (2009). CircStat: a MATLAB toolbox for circular statistics. J. Stat. Softw. *31*, 1–21.

100. Torrence, C., and Compo, G.P. (1998). A Practical Guide to Wavelet Analysis. Bull. Am. Meteorol. Soc. *79*, 61–78.

101. Fujisawa, S., Amarasingham, A., Harrison, M.T., and Buzsáki, G. (2008). Behavior-dependent short-term assembly dynamics in the medial prefrontal cortex. Nat. Neurosci. *11*, 823–833. https://doi.org/10.1038/nn.2134.

STAR★METHODS

KEY RESOURCES TABLE

REAGENT or RESOURCE	SOURCE	IDENTIFIER
Experimental models: Organisms/strains		
Mouse: C57BL/6J-Tg(Thy1-GCaMP6f)GP5.17Dkim/J	Jackson Laboratories	RRID: IMSR_JAX:025393
Software and algorithms		
MATLAB	Mathworks	https://www.mathworks.com/
Buzcode (MATLAB analysis tools)	Buzsaki Lab	https://github.com/buzsakilab/buzcode
FMA Toolbox (MATLABtoolbox for Freely Moving Animal (FMA))	Michael Zugaro	https://fmatoolbox.sourceforge.net/
Optical-flow analysis toolbox for wide-field neuroimaging	Majid Mohajerani	https://lethbridgebraindynamics.com/ofamm/
NIS Elements Imaging Acquisition Software	Nikon	https://www.microscope.healthcare.nikon.com/products/software/nis-elements
Other		
Silicon probes	Cambridge Neurotech, Diagnostic Biochips	H3 Probes
RHD2000 USB Interface Board	Intan Technologies	C3100
64 channel digital amplifiers	Intan Technologies	C3314
3D printed microdrives	Mihaly Voroslakos & Gyorgy Buzsaki	https://github.com/buzsakilab/3d_print_designs
Nikon AZ100 Macroscope	Nikon	https://www.microscopy.uk.com/sales/nikon-microscopes/nikon-az100-microscope

METHOD DETAILS

Animal handling

All experimental procedures were conducted in accordance with the National Institutes of Health guidelines and with the approval of the *New York University Grossman School of Medicine Institutional Animal Care and Use Committee (IACUC)*. C57BL/6J-Tg(Thy1-GCaMP6f) GP5.17Dkim/J (Jackson laboratories, Stock #:**025393**[40]) mice were used for all data collected; all males. Mice were kept in the vivarium on a standard 12-hour light/dark cycle and were housed 2-5 per cage before surgery and then alone following the surgery. Mice were provided food and water ad libitum throughout experiments, and experiments were conducted at the beginning of the light cycle to maximize sleep duration and quality.

Surgical procedures

Mice were anesthetized with isoflurane, homeothermically maintained, and monitored using pulse oximetry. In a fully aseptic environment, the scalp over the craniotomy area was resected. Skull thinning was then performed with constant saline irrigation, avoiding excessive drilling of the sutures but ensuring the removal of the outer and spongy bone layer. The thinning area extended over the entire dorsal right hemisphere, from the frontal cortex to the posterior visual cortex. Once drilled to translucency with only the inner compact bone layer remaining, the dry surface of the skull was coated with a thin layer of cyanoacrylate (gel-type Loctite Super Glue), which serves to index-match the rough surface of the skull, preventing bone re-growth and provide mechanical protection. The skin around the thinned skull preparation was sealed using cyanoacrylate tissue adhesive (e.g., 3MTM VetbondTM Tissue Adhesive). A thin coating of clear nail polish was then applied on top of the cyanoacrylate to further index-match the skull's surface and reduce scatter. Finally, a ground screw coupled with a 0.005" stainless steel wire (A- M Systems, #792800) was implanted in the skull above the cerebellum, and a custom 3d-printed head post was fixed to the surface of the skull using dental cement. Mice were then allowed to recover for one week and were inspected for response to visual stimuli to confirm the expected expression and dynamics of GCaMP6f.

In a second surgery, performed 5 days to one week following the first surgery, mice were implanted chronically with a 64-site or 128-site linear silicon probe (H3; Cambridge Neurotech) at a 60° angle, mounted onto a Cambridge Neurotech Nanodrive. The probe spanned deep (64-cite) or deep and superficial (128-cite) layers of retrosplenial cortex and area CA1 of the hippocampus ipsilateral to

the imaging field of view, after being lowered from a craniotomy at 0.5 mm DV and 2.95 mm AP coordinates in the contralateral (left) hemisphere (Figure 1). The probe and nanodrive were then enclosed in the remaining components of the 3d printed head-post.

Behavior

After recovery for 1 week, animals were gradually habituated to head fixation (modified rivets system[92]) for 5 to 7 days, where the amount of time spent head-fixed increased from 10 minutes to two hours. During both habituation and head-fixed experimental sessions, animals were free to run or rest on a 1.9-m length custom treadmill, during which no reward was delivered. Animal behavior was monitored during head-fixation using a small camera (Basler ace acA1300-60gm-NIR GigE Camera) under IR illumination, and a hall effects sensor (Littelfuse 55140-3H-02-A) placed at the axel of one treadmill wheel. Mice were encouraged to sleep using the following strategy: performing imaging sessions at the transition to their sleep cycle (i.e., daytime), increasing the force needed to move the treadmill but still allowing movement, and using a heated treadmill platform that partially enclosed their bodies. Home-cage sleep sessions allowed the mice to behave freely while plugged into the recording cable. Both head-fixed and home-cage setups were Faraday-protected using a metal mesh connected to the ground.

Electrophysiological Recordings

Electrophysiological recordings were conducted using an Intan RHD2000 interface board with sampling at 20 kHz (IntanTech). Signals were recorded in a unipolar manner against a reference and common ground (cerebellar screw) and digitized by a head-mounted preamplifier. Frame times for the behavior-recording camera and the widefield imaging camera signal were recorded as digital inputs to the Intan system. Probes were gradually lowered until sharp-wave ripple (SWR) depth profiles were clearly visible and then left in place for the duration of the experiment.

Widefield Recordings

Widefield imaging was performed on the right hemisphere of head-fixed mice through the thinned skull preparation using the MVX-10 Macroscope (Olympus) during simultaneous chronic electrophysiological recordings of ipsilateral retrosplenial cortex and CA1. Data were recorded using an Andor Zyla sCMOS camera with dual-wavelength LED imaging (cool LED PE-4000 system) and camera control by NIS Elements software (Nikon). 16-bit images were acquired at a rate of between 66.66 Hz and 100 Hz using global shutter mode. Alternating illumination between 470 nm and 525 nm on a per-frame basis was used in some cases, and illumination with a third wavelength at 630 nm was used for a small subset of videos. Illumination was collected via a 500-nm long pass emissions filter.

Histology

After experiments, mice were anesthetized with an injection of 150 mg/kg ketamine and 10 mg/kg xylazine. After checking for the absence of reflexes, animals were transcardially perfused by inserting a 27-gauge needle into the left ventricle of the heart while simultaneously severing the right atrium. Following perfusion with 1X PBS, 4% paraformaldehyde in PBS was circulated in the animal. The brain was removed and fixed overnight in 4% paraformaldehyde at 4°C and then sectioned into 60-μm thick horizontal slices using a microtome (Leica VT1000S) after washing to undergo immunohistochemistry. The slices were mounted on imaging slides in Vectashield Hard Set Mounting Medium with DAPI (Vector Laboratories). Brains were then imaged under a florescent microscope under 350 nm to capture DAPI and 470 nm wavelengths to capture the GCaMP signal.

DATA ANALYSIS

Data analysis was performed using custom software written in Matlab (MathWorks) and adapted from the Buzsaki Lab code repository (https://github.com/buzsakilab/buzcode).

Electrophysiological data preprocessing

Data files for paired head fixed and homecage recording sessions were concatenated and downsampled to 1250 Hz for LFP analysis.

Widefield data preprocessing

The following is adapted from Peters et al.[43]. All wide-field data were de-noised via compression using singular value decomposition of the form $F = USV^T$. The input to the SVD algorithm was F, the pixels x time matrix of fluorescence values. The outputs were U, the pixels x components matrix of template images; V, the time x components matrix of component time courses; and S, the diagonal matrix of singular values. The top 200 components were retained, found to be inclusive of a threshold determined by the Marchenko-Pastur distribution of a random matrix[93]; a more theoretically-motivated noise threshold, but ultimately more time extensive and unnecessary to compute given sufficient de-noising with 200 components. All orthogonally invariant operations (such as deconvolution, event-triggered averaging and ridge regression to predict cortical activity from the wide-field signal) were carried out directly on the matrix $\mathbf{S}^*\mathbf{V}$, allowing a substantial saving of time and memory.

Hemodynamic effects on fluorescence were removed by regressing out a green 525 nm widefield channel, reflecting changes in total blood volume, from the calcium-dependent signal obtained with blue illumination (470 nm). To achieve this, both signals were band-pass filtered in the range 7–13 Hz (heartbeat frequency, expected to have the largest hemodynamic effect). Pixel traces for blue

illumination (470 nm) were then temporally resampled to be concurrent with green illumination (525 nm, as colors were alternated), and a scaling factor for the given pixel-wise regression was fit across colors for each pixel. The scaled fluorescence traces from 525 nm green light illumination were then subtracted from the fluorescence traces emitted from 470 nm blue light illumination. To correct for slow drift, hemodynamic-corrected fluorescence was then high-pass filtered over 0.01 Hz and ΔF/F0-normalized by dividing by the average fluorescence at each pixel within the session.

Wide-field videos were then aligned across sessions by rigid registration of the average green-illuminated image to the Allen Common Coordinate Framework52[42] using two anatomical coordinates, lambda and bregma (marked during surgery). In a subset of mice, visual stimuli were presented and average deconvolved activity was confirmed to show a response in V1 (see Figures S1 and S2; Data S1). In all mice, the closest correlation with RSC population rate was in RSC, as expected.

In some cases, for very long videos, SVD was performed on segments of individual videos. When this was done, U matrices differed across sub-videos, leading to data reconstruction occurring across distinct principal axes. To combat any potential issues arising from this, all U matrices (200 components) were concatenated, and SVD was performed on this matrix; data were then reconstructed using this 'master' U matrix.

Fluorescence was deconvolved using a kernel fit from predicting retrosplenial cortical (RSC) multiunit activity from wide-field GCaMP6f fluorescence using ridge regression. This kernel was estimated by using simultaneous wide-field imaging and electrophysiological recordings in RSC. The single pixel with the highest correlation to the population rate before deconvolution was used for this purpose, and the population rate was calculated by binning spiking data for a spike-sorted session per mouse. 10-fold cross-validation was performed, and a lambda of 0.02 was used for regularization. The final deconvolution kernel was a mean of maximum-normalized kernels across recordings divided by the sum of squared weights across time. The deconvolution kernel was biphasic and roughly similar to a derivative filter (that is, [−1,1]), consistent with rises in the GCaMP signal corresponding to periods of spiking.

Analysis of traveling waves was performed using the Optical Flow Connectivity Toolbox.[94] Note that vector fields were computed using average SWR-triggered videos and thus denote changes in local widefield values from frame to frame on average, which may or may not be representative of individual trajectories. For our purposes, this is sufficient to give a sense of changes in activity over time on average.

Multiple unit activity (MUA) extraction

MUA extraction was implemented by MUAfromDat.mat (git: buzcode) via the following steps: First, a user-specified channel from the raw .dat file in the region of interest was band-pass filtered in the 500 to 5000 Hz frequency range. Then the estimated EMG from the LFP[96] was used to replace EMG-related artifacts with 'NaN' values. MUA was then normalized between 0 and 1 within each session. Two common methods of MUA extraction, MUA via band-pass filtering vs MUA via the pooling of spike-sorted units, were indistinguishable.

UP/DOWN state detection

DOWN states were detected using DetectSlowWavesMUA.mat (git: buzcode), parameters: smoothwin = 0.3, startbins = 40, refineDipEstimate = true. Briefly, MUA is detected as described above. If the distribution of the log-transformed MUA values are significantly bimodal (Hartigan's dip test), the trough of this bimodal distribution is identified (bz_BimodalThresh.mat), and anything above this threshold is regarded an UP state; below a DOWN state. A Schmidt trigger (threshold), which uses the halfway points between trough and upper peaks for onset and offset of a given state, was compared to a hard threshold, and no significant difference was found, as expected given the high data quality (Schmidt triggers are a useful control in noisy data).

Ripple detection and analysis

Ripples were detected as described previously,[95] using bz_FindRipples (git: buzcode). Briefly, the raw LFP (1250 Hz) was filtered (130-200 Hz; Butterworth; order = 3) and was transformed to a normalized squared signal (NSS). This signal was used to identify peaks beyond 5 standard deviations above the mean NSS. The beginning/end cutoff of the ripple was defined by a threshold of 2 standard deviations above the mean NSS. Ripple duration limits were between 15ms and 250ms. In addition, estimated EMG from the wide-band recording[96] was used to exclude EMG-related artifacts. The peak of the ripple (max power value > 5 standard deviations) was defined as time 0 for the ripple. Ripples were defined across the entire duration of a day, including both periods in the maze and the homecage. Ripple frequency was computed as the derivative of the ripple-band filtered LFP during ripple intervals found above. Ripple power is the power in the ripple band found via wavelet decomposition normalized by power in the ripple band during inter-ripple intervals. Sharp wave (SW) magnitude was the $\log_{10}$ normalized value of the sink after calculating the CSD across channels spanning the pyramidal cell layer using the inverse CSD method, which is based on the inversion of the electrostatic forward solution.[97] All SWRs were manually inspected, and any clearly resembling noise was excluded from the analysis.

Tonic MUA

Tonic MUA was computed by calculating the median deep RSC MUA across the duration of a given UP state. Each UP state has a single tonic MUA value.

Average variables across time normalized UP/DOWN states

Time normalized UP and DOWN states were computed by taking the median value of interest (RSC MUA, HPC MUA, P(SWR), amplitude SWR, P(burst onset SWR)) within 15 evenly spaced bins within either all UP states, or all DOWN states, and then averaging the value of interest across all time normalized UP states or time normalized DOWN states. Because number of bins was kept constant to allow averaging of variable duration UP and DOWN stats, bin time duration was variable.

Brain State Scoring

A previously described semi-automated sleep scoring algorithm was used.[20] It calculates a spectrogram from the raw LFP (1.25kHz) using a 10-s window FFT, sliding at 1 s intervals, at logarithmically spaced frequencies from 1 to 100 Hz. Briefly, this algorithm uses a set of heuristics when examining the EMG, theta band ratio (4-9 Hz divided by 2-16 Hz), and broadband LFP. The estimated EMG is the summed pairwise zero-lag correlation between non-neighboring electrodes (separate shanks; > 200um distance) using the band-pass filtered (300-600 Hz; 3rd order Butterworth) local field potential.[96] The theta band ratio is the 4-9 Hz power from the spectrogram divided by the 2-16 Hz power. The broadband LFP spectrogram was then compressed using principal components analysis (PC1 always corresponding to < 20Hz power). The algorithm then uses these data in a sequence of separations, finding troughs that maximally split peaks in each distribution. In all recordings, manual inspection of scoring was conducted. In some cases, manual curation of algorithm parameters or specific segments of recordings was conducted to identify brain state best.

PSS Power spectrum slope (PSS)

We used the power spectrum slope as an estimate for brain state and as a potential index of cortical E/I balance.[45] For each session, we selected an infragranular cortical channel and extracted the slope of the power spectrum between 4-100 Hz in a 2 seconds interval and a 50 ms sliding window. PSS describes state changes as a single value. Its relationship to classically defined brain state changes can be calibrated and PSS values can then be assigned to these discrete (arbitrary threshold-separated) states. While Brain State scoring provides isolated clouds for active waking (locomotion) and REM sleep, the relationship between quiet awake immobility and NREM sleep is more of a continuum than bimodally separable states.[98]

Computing SWR phase-relationship with infraslow blood flow signal

Every neocortical pixel in the 520 nm wavelength (green) channel was filtered in the infraslow frequency range, [.04 to .5] Hz. The phase angles for each timestamp when a SWR peak occurred within NREM epochs were then calculated separately for each pixel using the real component of the Hilbert transform and plotted in a histogram. The circular mean and resultant vector were then calculated using these histograms for each widefield pixel.[99] For a null distribution, widefield infraslow phase angles were circularly shifted by a random offset and the phase angle histograms were then recalculated (10 iterations). Resultant p-values are calculated based on this bootstrapped null distribution and plotted for each pixel.

Spectrograms x infraslow phase

We first concatenated all NREM epochs for a given session within mouse of a select LFP channel, either from deep-layer RSC or the CA1 pyramidal cell layer. We then calculated a time-resolved wavelet spectrogram by convolving this LFP time series with a family of complex Morlet wavelets,[100] $\log_2$-spaced between 1 and 200 Hz with variable time resolution, allowing for fixed five cycles per frequency. The wavelet spectrogram was then mean-normalized within frequency. Next, we plotted the average power spectrum by infraslow phase (Figure S4G) by assigning an instantaneous phase of total blood volume (520 nm channel) filtered in the infraslow frequency range (0.04 to 0.5 Hz), to each time-point in the spectrogram, sorting the spectrogram into 20 evenly spaced phase-bins, and then averaging across time within those bins. This allowed us to visualize changes in the power spectrum for the given LFP by phase infraslow (see bz_LFPSpecToExternalVar).

Identification of SWR types

In main Figure 4, we observe asymmetric clustering of SWRs around U-D and D-U transitions and ultimately identify four SWR "types" based on their proximity to the nearest U-D and D-U transition: SWR_U, SWR_{UD}, SWR_D, and SWR_{DU}. We note that the SWR_{UD} and SWR_{DU} are partially overlapping categories, as a SWR can both follow a D-U transition at a specific latency and occur just before a U-D transition. For the purpose of our study, grouping SWRs into overlapping categories is not problematic, as we are ultimately testing the hypothesis of bidirectional interaction between regions and do not group SWRs by "type" for the analyses in main Figures 5, 6, or 7. We elaborate on our classification of SWR types in Figure S5. First, we plotted the distribution of the latency of the specified SWRs from four time points: the latency of all UP SWRs to the closest previous U-D transition (Figure S5B), the latency of all DOWN SWRs following the closest previous U-D transition (Figure S5C), the latency of all DOWN SWRs to the next D-U transition (Figure S5D), and the latency of all UP SWRs from the previous DOWN-UP transition (Figure S5E). From these distributions, latency cut-offs were determined based on peaks in the latency distributions, latency intervals noted on plots, the colors in Figures S5B–S5E corresponding to the outlined peaks in P(SWR) in Figure S5A. SWR_{UD} in category 'A' (red) occurred within 40 ms of the U-D transition, SWR_{DU} (green) in category 'E' occurred between 50 and 180 ms post-D-U transition, SWR_U in category 'F' (yellow) occurred during an UP state between 180 to 200 ms following a D-U transition, and SWR_D in category 'B' (magenta) occurred between 1 to 80 ms following the U-D transition.

In Figures S5F and S5G, we assign every SWR to one of 9 non-overlapping categories defined by their proximity to the closest U-D and D-U transitions (numbered 1-9), specified by the combinations of latency intervals below each plot (more generally – how far is a SWR from the nearest U-D and D-U transition, and how long is the UP state within which it occurs). Categories 1-7 occur during the UP state, and 8-9 during the DOWN state. Categories 1-3 comprise SWR_{UD}, category 5 SWR_{DU}, category 8 SWR_{D}, and categories 6 and 7 SWR_{U}. In Figure S5H, we present SWR raster plots of each SWR type surrounding the D-U transition, colored by the amplitude of the SWRs. We note the four major SWR types whose potential functions we discuss in the manuscript.

Calculation of DOWN states in widefield data

Deconvolved widefield data was binarized into putative UP and DOWN states by thresholding each pixel by its 25th percentile value, above which was an UP state and below which a DOWN state. The 25th percentile was chosen because it maximized the KS-distance between RSC MUA values during RSC widefield detected UP vs DOWN states (Figure S7A). In more detail, we detected putative DOWN states in RSC widefield time series using thresholds evenly spaced between 15 and 40th percentiles, leading to variation in identified DOWN onsets and offsets. We then leveraged our simultaneous RSC widefield and electrophysiological recordings by computing the distribution of RSC MUA values in each of the widefield-determined putative UP and DOWN states (pooled across all videos within a given mouse to control for variation in depth of NREM). The value with the greatest distance between detected UP and DOWN states was the 25th percentile threshold. We then calculated the 25th percentile value for each pixel within each mouse, and applied this threshold to that pixel's time series to identify UP and DOWN states. Although we could only perform the above electrophysiologically-determined widefield threshold within RSC, we found no systematic bias in computed 25th percentile values across regions (Figures S7B and S7C), as expected assuming an approximately uniform imaging quality.

Given the lower temporal (and thus spatial) resolution of this datatype, we performed an additional quality check, wherein we evaluated changes in DOWN detection quality (operationalized as UP vs DOWN KS-distance) as a function of DOWN duration deciles for RSC and M1 ROIs (Figures S7D–S7F). In short, for the specified ROIs (Figure 7F), DOWN states were split into duration deciles, from short to long. Then, two KS-values were computed (dotted and solid lines in Figure S7E), addressing two distinct questions. First, we asked whether the widefield DOWN detection quality is similar across regions as DOWN state duration varies (dotted lines). It is possible that although long, and thus global, DOWN states are easily detected across regions, shorter duration (and thus local) DOWN states may be missed in regions not central to our investigation. This could be problematic for analyses that vary the duration of DOWN states, such as computing SWR modulation indices. This control analysis was thus done by computing the KS-distance between distributions of UP and DOWN widefield values, for the given pixel, at each duration DOWN decile. Across regions, KS-distances remained similar regardless of duration DOWN – suggesting minimal variation in detection quality (Figures S7E and S7F, dotted lines).

A second question can be addressed given our concurrent electrophysiological and widefield recordings in RSC - does widefield DOWN detection quality vary with DOWN duration if using RSC MUA. Ideally, when calculating KS-distances using RSC widefield-detected DOWN states to bin RSC MUA into 'UP' and 'DOWN' distributions, we would see minimal change in KS-distance, as is true when using electrophysiologically-detected DOWN states to bin RSC MUA (Figure S7F, black line). However, we instead observed an increase in KS-distance with increasing DOWN duration, meaning a systematic improvement in detection quality. This is unsurprising, as it reflects the temporal resolution of widefield data. Fortunately, for our purposes, we exclude DOWN states shorter than 80 ms in duration in order to avoid including other silent events (e.g., 4Hz or spindles) in our results. Overall, even if short-duration DOWN states are less effectively resolved, comparisons across regions remain sound given the equivalent quality of DOWN state detection across regions using widefield time series.

DOWN state modulation index

For every pixel, DOWN states detected for the given pixel were divided into duration quintiles, from short to long. For each quintile, a DOWN state modulation index was computed by dividing the total number of SWRs observed during UP states minus DOWN states, divided by the sum of SWRs in those same UP states and DOWN states. To compensate for the variable duration of UP and DOWN states, SWRs were summed only within a 70ms window from the end of each UP state, and end of each DOWN state. (Note: DOWN states with less than 80ms duration were excluded to avoid mid-identification of spindle troughs). Modulation indices were averaged across mice, resulting in one modulation index per pixel (Figure 6C), or one modulation index per pixel per DOWN duration quintile (Figure S6G), plotted in a map in Figure 6E.

Cross-correlograms of widefield data

The probability of DOWN states surrounding SWRs (Figures 7Ai and 7Bi) and SWRs surrounding U-D and D-U transitions (Figure 7Ci) was quantified by calculating the cross-correlation between the trigger of interest for a given pixel, SWR peaks sorted by amplitude and D-U transitions respectively, pooled across all mice. This provided a unique map in time, showing the probability of DOWN state transitions across regions surrounding SWRs (Figure 7Ai) or probability SWRs in a single hippocampal location with respect to U-D and D-U transitions across all regions at fixed lags from those transitions (Figure 7Ci). The frames in Figures 7Ai, 7Bi, and 7Ci are still pictures taken from the videos in Videos S4 and S5. Data in Figure 7 are thresholded by a 95th percentile bootstrapped confidence interval for each pixel, constructed by re-computing the cross-correlograms of interest n=500 times.

Computing cross-correlograms to test whether the strength of input impacts population-level state transition in downstream region

We tested the hypothesis that the hippocampus and RSC can bi-directionally "kick" one another by computing cross-correlograms between putative input variables (in the hippocampus to RSC direction: SWRs; in the RSC to hippocampus direction: D-U transitions) and putative response variables (hippocampus to RSC: DOWN states; RSC to hippocampus: SWRs), by reasoning that the larger the input variable, the greater the probability of evoking a state transition in the downstream region. We thus split the input into octiles that varied by input "strength", operationalized as the amplitude of SWRs or magnitude of synchrony at the D-U transition, for hippocampus and RSC, respectively. For each cross-correlogram (CCG) between input times of a given input strength octile and all response times, surrogate data sets were constructed by randomly and independently jittering timestamps on a uniform interval of [-20, 20] ms 1000 times. 99% confidence intervals were then calculated for each time bin, plotted as shaded regions along the CCGs in Figures 5B and 5E.[101] The larger the SWR octile, the higher the probability of a DOWN state following that SWR octile at a fixed lag of 30ms±15 ms. The larger the synchrony, the higher the probability of a SWR following the transition at a fixed lag of 120ms±15 ms. For all CCGs in Figure 5, time series were combined across animals and variations in input strength were denoted with deepening color (light pink to dark red; or light green to dark green). The same conclusions can be drawn from cross-correlograms of individual mice, suggesting strong evidence of short-timescale bi-directional interaction between hippocampus and RSC via coordinated state transitions.

Testing the effect of input strength and state of downstream region on probability of evoking a population-level state transition via repeated measures ANOVA

We next tested for the effect of two independent variables and their interaction on the probability of evoking an RSC DOWN state. For this analysis, we binned SWRs not just by input strength octiles, but also by the arousal level of the animal, taken to be PSS value when a given trigger, a SWR or D-U transition, occurred. Given the fixed lag at which DOWN states occur in response to increasingly large SWRs (30±15 ms), we computed CCGs for each condition, computed a two-way repeated measures ANOVA with values of each CCG at this time bin, and tested for a significant effect of amplitude SWR, state, and their interaction at the session level across mice. As expected, we found a significant effect of both factors and their interaction; the higher the PSS value (corresponding to deeper NREM sleep) and larger the SWR, the higher the probability of an evoked DOWN state. These effects were lost at a control time lag of 200 ms. We followed this same logic in the RSC to hippocampus direction and found a significant effect of both magnitude synchrony, PSS value at the time of the trigger, and their interaction in probability of evoking a SWR at a lag of 120 ms (two-way repeated measures ANOVA). At a control lag of 350 ms, we found a significant effect of local state but not strength input on probability of SWR occurrence.

Predicting duration DOWN state or magnitude of sharp wave using input strength and local state as predictors in a generalized linear model

In events where a DOWN state followed a SWR (SWR_{UD}), we tested whether the duration of the DOWN state varied with state, in this case, PSS, and input strength (i.e., SWR amplitude) using a generalized linear model with both variables (PSS and SWR amplitude) and their interaction as predictors, and duration DOWN state as the response variable. In this case, we did not bin PSS or SWR amplitude and only performed this binning with average duration DOWN for visualization of results. We found a significant effect of both predictors and their interaction. When we took all SWRs during the UP state and repeated this process for the following DOWN state (rather than just SWRs with a putative causal impact on cortical DOWN state given their occurrence just prior), amplitude SWR was no longer predictive of duration DOWN, further supporting our causal hypothesis. Note, however, that we only found a significant effect of state using PSS, reflecting global arousal level, rather than local state.

In those cases where a SWR followed a transition from a D-U state, we tested whether the magnitude of the sharp wave, reflecting putative degree of input, depended on the strength of the input and state, by using synchrony at the D-U transition, PSS, and their interaction as predictors using the same GLM framework. We found a significant effect of state, but not of strength input or the interaction between the two predictor variables. This suggests that magnitude SW is determined largely by local excitability, which is presumed to change with depth sleep, rather than strength input.

Statistical methods

Mean or medians are given with std. dev. Significance testing of data comparisons was done by standard parametric (Student's t test) and non-parametric (Wilcoxon signed-rank or rank-sum tests) tests or by determining the crossings of confidence boundaries of surrogate datasets (compensated for type I statistical error). Multiple comparisons were corrected using Tukey-Kramer post hoc test. No statistical methods were used to predetermine sample sizes; however, sample sizes were similar or larger than those generally employed in the field. Data collection and analysis were not performed blind to the conditions of the experiments and no randomization was used.

MODEL SETUP

The model comprises of two local circuits, one representing the Retrosplenial Cortex (RSC) and the other the Hippocampus (HPC), interconnected through long range projections. The dynamics of neural activity in each of the two regions is described through the mean firing rate of an inhibitory and an excitatory population[34]. The excitatory population of the RSC is subject to a hyperpolarization-activated

current I_h [62] whereas the excitatory population of the HPC is subject to an adaptive current[34,59]. This is summarized by the vector equations:

$$\boldsymbol{\tau_r}\dot{\boldsymbol{r}} = -\boldsymbol{r} + R_\infty(\boldsymbol{W}\boldsymbol{r} + \boldsymbol{b}\boldsymbol{a} + \boldsymbol{I} + \boldsymbol{\zeta}(t)) \quad \text{(Equation 1)}$$

$$\boldsymbol{\tau_a}\dot{\boldsymbol{a}} = -\boldsymbol{a} + A_\infty(\boldsymbol{r}) \quad \text{(Equation 2)}$$

where:

- $\boldsymbol{\tau_r}$ is a vector whose entries represent the time constant for each population. We set them all equal to 1 for simplicity, time is thus dimensionalized to units of the population rate constant.
- $\boldsymbol{r} = \begin{bmatrix} r_E^C \\ r_I^C \\ r_E^H \\ r_I^H \end{bmatrix}$ is a vector of firing rates of the excitatory and inhibitory populations of cortex (r_E^C, r_I^C) and hippocampus (r_E^H, r_I^H).
- $\boldsymbol{W} = \begin{bmatrix} w_{EE}^{CC} & w_{EI}^{CC} & w_{EE}^{CH} & 0 \\ w_{IE}^{CC} & w_{II}^{CC} & w_{IE}^{CH} & 0 \\ w_{EE}^{HC} & 0 & w_{EE}^{HH} & w_{EI}^{HH} \\ w_{IE}^{HC} & 0 & w_{IE}^{HH} & w_{II}^{CC} \end{bmatrix}$ is the matrix of connection strengths between populations, such that w_{EE}^{CH} represents the projections strength from population E of region H (Hippocampus) to population E of region C (Cortex). For long-range projections, e.g. originating in HPC and terminating in RSC, we include a 10ms delay transmission to simulate the effects of synaptic transmission between separate brain regions. Note: In this case $w_{EI}^{CH}, w_{II}^{CH}, w_{EI}^{HC}, w_{II}^{HC}$ are set to zero, as we only include long-range projections originating in excitatory neurons in each region.
- $\boldsymbol{b} = \begin{bmatrix} b_E^C \\ 0 \\ b_E^H \\ 0 \end{bmatrix}$ is the vector of a strengths onto respective populations.
- $\boldsymbol{a} = \begin{bmatrix} a_E^C \\ 0 \\ a_E^H \\ 0 \end{bmatrix}$ is the vector of adaptive current for each population (I_h for RSC and a for HPC).
- $\boldsymbol{I} = \begin{bmatrix} I_E^C \\ I_I^C \\ I_E^H \\ I_I^H \end{bmatrix}$ is the vector of background tonic input to each population.
- $\boldsymbol{\zeta}(t) = \begin{bmatrix} \zeta_{E,(t)}^C \\ \zeta_{I,(t)}^C \\ \zeta_{E,(t)}^H \\ \zeta_{I,(t)}^H \end{bmatrix}$ is the time-dependent vector of Ornstein-Uhlenbeck (OU) noise which is applied to each population. This is given by:

$$d\zeta = -\frac{\zeta}{\tau}dt + \sigma\sqrt{\frac{2}{\tau}}dtW_t \quad \text{(Equation 3)}$$

where W_t is a Weiner process. Here we use the standard deviation $\sigma = 0.37$ and time scale $\tau = 20$.

- $\boldsymbol{\tau}_a$ is a vector containing the time constants for a in each excitatory population. For simplicity these are identical in both the cortical and the hippocampal population.
- $R_{\gamma,\infty} = g_\gamma[x - \theta_\gamma]_+^2, \gamma = E, I$ represents the threshold-quadratic activation function for each excitatory and inhibitory population. g and θ are chosen such that $\theta_E < \theta_I$ and $g_E < g_I$, which are necessary conditions for 3 steady states in the phase plane dynamics of each local circuit[59].
- $A_\infty = \frac{1}{1+e^{-k(r-r_0)}}$ represents the sigmoid activation function of a current for each population and depends on two parameters k and r0. Note that for positive k this is an adaptive current which grows during periods of high firing, whereas for negative k, this is an inactivity-activated current.

Model implementation

Simulations for Equations 1 and 2 are performed in Matlab using the dde23 solver, with OU noise precomputed independently using the forward Euler method with time step $dt = 0.01$ and a delay of 10ms between inputs arriving via long-range projections from the two regions. Because dde23 uses a variable time step to approximate the solution to the differential equations, we interpolate the solution at every 1ms time-step, making it comparable to sampling frequency of the experimental data. Final simulation statistics are determined for 10^6 time-steps, in order to have a similar number of UP and DOWN states as the experimental data.

Local Connection Strengths

The dynamics of the local circuit depend on the particular choices of local parameters W and I. To determine the parameters that best fit the dynamics of the biological regions we perform a parameter search across variables W_{EE}(local recurrence) and I (background input). Note: For simplicity, we set $W_{IE} = W_{EE} + 0.2$ and $I_I = I_E - 0.2$. We then compare state duration statistics (UP and DOWN states for CTX and SWR and iSWR states for HPC) for simulations with the experimental data by calculating the Kolmogorov–Smirnov (KS) statistic between the two distributions, as in Levenstein et al.,[34] and define an overall similarity between data and model as:

$$Similarity_{CTX} = (1 - KS_{DOWN})(1 - KS_{UP}) \quad \text{(Equation 4)}$$

$$Similarity_{HPC} = (1 - KS_{iSWR})(1 - KS_{SWR}) \quad \text{(Equation 5)}$$

Best parameter fit was defined for parameters that gave the highest similarity between model and data.

Long Range Connection Strengths

As for local connection strengths, we perform a parameter search in both $E \rightarrow E$ and $E \rightarrow I$ projection strengths and compare simulation outputs to data. We separately test $RSC \rightarrow HPC$ projections and $HPC \rightarrow RSC$ projection to verify the causal effect of RSC UP and DOWN states in HPC MUA tonic modulation and rebound excitation on P(SWR) after a DOWN to UP transition in RSC, as well as the perturbation effect that SWR from the HPC have on the RSC inducing DOWN state transitions. Overall, we select final Long-Range parameters such that they satisfy the following criteria:

- Maintain closest fit to data UP and DOWN state duration statistics.
- Show tonic modulation of HPC MUA by RSC UP and DOWN states, such that HPC MUA is lower during a cortical DOWN state and higher during a cortical UP state.
- Maximize P(SWR) at the UP to DOWN and DOWN to UP transitions.

Model Parameters

Final model parameters for Equations 1 and 2 are summarized in the following table:

Parameter	Value
Connection strengths $\begin{bmatrix} w_{EE}^{CC} & w_{EI}^{CC} & w_{EE}^{CH} & 0 \\ w_{IE}^{CC} & w_{II}^{CC} & w_{IE}^{CH} & 0 \\ w_{EE}^{HC} & 0 & w_{EE}^{HH} & w_{EI}^{HH} \\ w_{IE}^{HC} & 0 & w_{IE}^{HH} & w_{II}^{CC} \end{bmatrix}$	$\begin{bmatrix} 3.04 & -1.5 & 0.13793 & 0 \\ 3.24 & -0.5 & 0.724137 & 0 \\ 0.103448 & 0 & 2.83 & -1.5 \\ 0.068965 & 0 & 3.03 & -0.5 \end{bmatrix}$

(Continued on next page)

Continued

Parameter	Value
b_E^C, b_I^C	$-0.8, 0.8$
$I_E^C, I_I^C, I_E^H, I_I^H$	$3.35, 2.72, 3.36, 2.77$
τ_h	100
g_E, g_I	$0.02, 0.05$
θ_E, θ_I	$0, 12$
r_0	2
k^C, k^H	$-20, 20$